

## MnO<sub>x</sub>-Promoted PdAg Alloy Nanoparticles for the Additive-Free Dehydrogenation of Formic Acid at Room Temperature

Ahmet Bulut, Mehmet Yurderi, Yasar Karatas, Zafer Say, Hilal Kivrak,  
Murat Kaya, Mehmet GÜLCAN, Emrah Ozensoy, and Mehmet Zahmakiran

*ACS Catal.*, **Just Accepted Manuscript** • DOI: 10.1021/acscatal.5b01121 • Publication Date (Web): 09 Sep 2015

Downloaded from <http://pubs.acs.org> on September 13, 2015

### Just Accepted

“Just Accepted” manuscripts have been peer-reviewed and accepted for publication. They are posted online prior to technical editing, formatting for publication and author proofing. The American Chemical Society provides “Just Accepted” as a free service to the research community to expedite the dissemination of scientific material as soon as possible after acceptance. “Just Accepted” manuscripts appear in full in PDF format accompanied by an HTML abstract. “Just Accepted” manuscripts have been fully peer reviewed, but should not be considered the official version of record. They are accessible to all readers and citable by the Digital Object Identifier (DOI®). “Just Accepted” is an optional service offered to authors. Therefore, the “Just Accepted” Web site may not include all articles that will be published in the journal. After a manuscript is technically edited and formatted, it will be removed from the “Just Accepted” Web site and published as an ASAP article. Note that technical editing may introduce minor changes to the manuscript text and/or graphics which could affect content, and all legal disclaimers and ethical guidelines that apply to the journal pertain. ACS cannot be held responsible for errors or consequences arising from the use of information contained in these “Just Accepted” manuscripts.



1  
2  
3  
4  
5  
6  
7 MnO<sub>x</sub>-Promoted PdAg Alloy Nanoparticles for the  
8  
9  
10  
11 Additive-Free Dehydrogenation of Formic Acid at  
12  
13  
14  
15 Room Temperature  
16  
17  
18  
19  
20

21 *Ahmet Bulut,<sup>†</sup> Mehmet Yurderi,<sup>†</sup> Yasar Karatas,<sup>†</sup> Zafer Say,<sup>‡</sup> Hilal Kivrak,<sup>§</sup> Murat Kaya,<sup>¥</sup>*

22  
23 *Mehmet Gulcan,<sup>†</sup> Emrah Ozensoy,<sup>‡</sup> Mehmet Zahmakiran<sup>\*†</sup>*  
24  
25

26  
27 <sup>†</sup> Nanomaterials and Catalysis (NanoMatCat) Research Laboratory, Department of Chemistry,  
28

29 Yüzüncü Yıl University, 65080, Van, Turkey; <sup>‡</sup> Department of Chemistry, Bilkent University,  
30

31 06800, Ankara, Turkey; <sup>§</sup> Department of Chemical Engineering, Yüzüncü Yıl University, 65080,  
32

33 Van, Turkey; <sup>¥</sup> Department of Chemical Engineering and Applied Chemistry, Atılım  
34

35  
36 University, 06836, Ankara, Turkey  
37  
38  
39  
40  
41  
42  
43  
44  
45  
46  
47  
48  
49  
50  
51  
52  
53  
54  
55  
56  
57  
58  
59  
60

**ABSTRACT**

Formic acid (HCOOH) has a great potential as a safe and a convenient hydrogen carrier for fuel cell applications. However efficient and CO-free hydrogen production through the decomposition of formic acid at low temperatures ( $< 363$  K) in the absence of additives constitutes a major challenge. Herein, we present a new heterogeneous catalyst system comprised of bimetallic PdAg alloy and  $\text{MnO}_x$  nanoparticles supported on amine-grafted silica facilitating the liberation of hydrogen at room temperature through the dehydrogenation of formic acid in the absence of any additives with remarkable activity ( $330 \text{ mol H}_2 \cdot \text{mol catalyst}^{-1} \cdot \text{h}^{-1}$ ) and selectivity ( $> 99 \%$ ) at complete conversion ( $> 99 \%$ ). Moreover this new catalytic system enables facile catalyst recovery and very high stability against agglomeration, leaching and CO poisoning. Through a comprehensive set of structural and functional characterization experiments, mechanistic origins of the unusually high catalytic activity, selectivity and stability of this unique catalytic system are elucidated. Current heterogeneous catalytic architecture presents itself as an excellent contender for clean hydrogen production via room-temperature additive-free dehydrogenation of formic acid for on-board hydrogen fuel cell applications.

Keywords: Formic Acid; Palladium; Silver; Alloy; Manganese; Dehydrogenation.

## INTRODUCTION

Hydrogen (H<sub>2</sub>) is considered to be a promising energy carrier due to its high energy density (142 MJ/kg), which is almost three times higher than that of natural gas (55 MJ/kg).<sup>1,2</sup> Furthermore, hydrogen is also an environmentally friendly energy vector as the utilization of hydrogen in proton exchange membrane fuel cells (PEMFC) generates only water as the chemical product.<sup>3</sup> However, controlled storage and release of hydrogen are still among the critical technological barriers faced by the hydrogen economy.<sup>1-3</sup> In this context, formic acid (HCOOH, FA), which is one of the major stable and non-toxic products formed in biomass processing, has recently attracted significant attention as a potential hydrogen carrier for fuel cells designed towards portable use.<sup>4,5</sup> In the presence of metal catalysts, FA can catalytically be decomposed via dehydrogenation (**1**) and/or dehydration (**2**) pathways.



The selective dehydrogenation of FA is vital for the production of ultrapure H<sub>2</sub>, since toxic carbon monoxide (CO) produced by the dehydration pathway significantly reduces the activity of the precious metal catalysts in PEMFC.<sup>6</sup> Recently, serious efforts have been focused on the development of homogeneous catalysts for the selective dehydrogenation of FA.<sup>7-11</sup> Even though notable catalytic performances have been reported in some of these studies,<sup>12-14</sup> the significant challenges associated with the catalyst isolation and recovery processes substantially hinder the practical use of such systems in on-board applications. Along these lines, numerous recent studies focused on the development of practical heterogeneous catalysts<sup>15-26</sup> exhibiting significant activity under mild conditions with high selectivity and facile catalyst recovery

1  
2  
3 capabilities. In spite of these numerous former efforts, the majority of the heterogeneous  
4 catalysts reported in the literature for FA dehydrogenation require elevated temperatures and the  
5 utilization of extra additives (*e.g.* HCOONa, NR<sub>3</sub>, LiBF<sub>4</sub> etc.),<sup>27-29</sup> while revealing low turnover  
6 frequency (TOF) values and limited reusability.<sup>16-18,20-22</sup> Until now, only a few Pd based  
7 heterogeneous catalysts have been found to provide notable activities in the additive-free FA  
8 dehydrogenation at low temperatures.<sup>19,23-25</sup> In this regard, the development of highly active,  
9 selective and reusable solid catalysts operating at low temperatures in the additive-free  
10 dehydrogenation of FA bears an enormous technological importance. Of particular importance,  
11 our recent study<sup>24</sup> has showed that Pd and MnO<sub>x</sub> nanoparticles existing as a physical mixture on  
12 the surface of amine-grafted silica catalyze the additive-free FA dehydrogenation with 82 %  
13 conversion and at room temperature. Moreover, the kinetic control experiments coupled with  
14 spectroscopic and electrochemical studies have led to the following important insights; (*i*) MnO<sub>x</sub>  
15 nanoparticles (NPs) act as CO-sponges around the catalytically active Pd NPs and improve their  
16 operational performance in the FA dehydrogenation, (*ii*) the surface grafted amine groups on  
17 SiO<sub>2</sub> support enhance the activity of Pd NPs by influencing the FA adsorption/storage process as  
18 well as the nucleation and growth of the Pd and MnO<sub>x</sub> nanoparticles. These important findings  
19 have fostered us to use MnO<sub>x</sub> and amine-grafted SiO<sub>2</sub> support for the development of new Pd-  
20 based heterogeneous catalytic systems for the additive-free dehydrogenation of FA.  
21  
22  
23  
24  
25  
26  
27  
28  
29  
30  
31  
32  
33  
34  
35  
36  
37  
38  
39  
40  
41  
42  
43  
44  
45

46 Along these lines, in this study we present a facile synthetic route for obtaining PdAg alloy  
47 and MnO<sub>x</sub> NPs supported on aminopropyl-functionalized silica, which will hereafter be referred  
48 to as PdAg-MnO<sub>x</sub>/N-SiO<sub>2</sub>. Furthermore, we show the remarkable catalytic performance of this  
49 novel material architecture in the additive-free decomposition of FA at room temperature via  
50 pathway (**1**) with high reusability performance. PdAg-MnO<sub>x</sub>/N-SiO<sub>2</sub> catalyst was prepared with  
51  
52  
53  
54  
55  
56  
57  
58  
59  
60

1  
2  
3 high reproducibility through a simple impregnation route followed by subsequent sodium  
4 borohydride ( $\text{NaBH}_4$ ) reduction in water at room temperature. The structural characterization of  
5  
6 PdAg-MnO<sub>x</sub>/N-SiO<sub>2</sub> was performed by using a multitude of analytical techniques including  
7  
8 inductively coupled plasma-optical emission spectroscopy (ICP-OES), powder X-ray diffraction  
9  
10 (XRD), *in-situ* Fourier transform infrared spectroscopy (*in-situ* FTIR), X-ray photoelectron  
11  
12 spectroscopy (XPS), diffuse reflectance UV-Vis (DR-UV-Vis) spectroscopy, transmission  
13  
14 electron microscopy (TEM), high resolution transmission electron microscopy (HRTEM),  
15  
16 scanning transmission electron microscopy-energy dispersive X-ray spectroscopy (STEM-EDX),  
17  
18 high angle annular dark field-scanning transmission electron microscopy (HAADF-STEM),  
19  
20 linear sweep voltammetry (LSV), CO-stripping voltammetry and N<sub>2</sub>-adsorption-desorption  
21  
22 techniques. Comprehensive structural characterization efforts presented in the current  
23  
24 contribution indicate the presence of separate PdAg alloy and MnO<sub>x</sub> NPs, which nucleate on the  
25  
26 surface of the aminopropyl-functionalized silica support surface and interact efficiently in a  
27  
28 synergistic manner. The resulting PdAg-MnO<sub>x</sub>/N-SiO<sub>2</sub> material can catalyze dehydrogenation of  
29  
30 FA in the absence of additives with the high activity (turnover frequency (TOF) = 330 h<sup>-1</sup>) even  
31  
32 at room temperature. Moreover, the exceptional durability of PdAg-MnO<sub>x</sub>/N-SiO<sub>2</sub> against  
33  
34 agglomeration, leaching and CO poisoning renders this catalytic architecture an excellent  
35  
36 contender as a reusable heterogeneous catalyst in the hydrogen production from formic acid for  
37  
38 on-board fuel cell applications.  
39  
40  
41  
42  
43  
44  
45  
46  
47  
48

## 49 **EXPERIMENTAL SECTION**

50  
51  
52 **Materials.** Palladium(II) nitrate dihydrate ( $\text{Pd}(\text{NO}_3)_2 \cdot 2\text{H}_2\text{O}$ ) (~ 40 % Pd basis), manganese(II)  
53 nitrate tetrahydrate ( $\text{Mn}(\text{NO}_3)_2 \cdot 4\text{H}_2\text{O}$ ), silver(I) nitrate ( $\text{AgNO}_3$ ), aminopropyltriethoxysilane  
54  
55 ( $\text{H}_2\text{N}(\text{CH}_2)_3\text{Si}(\text{OC}_2\text{H}_5)_3$ , APTS), sodium borohydride ( $\text{NaBH}_4$ ), ninhydrin ( $\text{C}_9\text{H}_6\text{O}_4$ ), toluene  
56  
57  
58  
59  
60

1  
2  
3 (C<sub>7</sub>H<sub>8</sub>) and sodium hydroxide (NaOH) were purchased from Sigma-Aldrich<sup>®</sup>. Formic acid  
4  
5 (CH<sub>2</sub>O<sub>2</sub>, > 96 %), and silica gel (230-400 mesh) were purchased from Merck<sup>®</sup>. Toluene was  
6  
7 distilled over sodium and stored in a Labsconco nitrogen-atmosphere drybox (O<sub>2</sub> < 1 ppm).  
8  
9 Deionized water was distilled by water purification system (Milli-Q Water Purification System).  
10  
11 All glassware and teflon-coated magnetic stirring bars were washed with acetone and copiously  
12  
13 rinsed with distilled water before drying in an oven at 423 K.  
14  
15  
16  
17  
18

19 **Characterization.** Pd, Ag and Mn contents of the samples were determined by ICP-OES  
20  
21 (Leeman, Direct Reading Echelle) after each sample was completely dissolved in a mixture of  
22  
23 HNO<sub>3</sub>/HCl (1/3 v/v). Powder X-ray diffraction (XRD) patterns were recorded with a MAC  
24  
25 Science MXP 3TZ diffractometer using Cu-K $\alpha$  radiation (wavelength 1.54 Å, 40 kV, 55 mA).  
26  
27 TEM, HRTEM, STEM, and HAADF-STEM samples were prepared by dropwise addition of the  
28  
29 dilute catalyst suspension on a copper-coated carbon TEM grid followed by the evaporation of  
30  
31 the solvent. The conventional TEM measurements were carried out on a JEOL JEM-200CX  
32  
33 transmission electron microscope operating at 120 kV. HRTEM, STEM and HAADF-STEM  
34  
35 analysis were performed using a JEOL JEM-2010F transmission electron microscope operating  
36  
37 at 200 kV. Oxford EDX system and the Inca software were exploited to acquire and process  
38  
39 STEM-EDX data. The XPS measurements were employed via a Physical Electronics 5800 XP  
40  
41 spectrometer equipped with a hemispherical analyzer and a monochromatic Al-K $\alpha$  X-Ray source  
42  
43 (1486.6 eV, 15 kV, 350 W, with pass energy of 23.5 eV). Gas phase decomposition products of  
44  
45 formic acid were analyzed by gas chromatography using FID-2014 and TCD-2014GC analyzers  
46  
47 (Shimadzu). UV-Vis electronic absorption spectra were recorded on a Shimadzu UV-2600  
48  
49 spectrophotometer.  
50  
51  
52  
53  
54  
55  
56  
57  
58  
59  
60

1  
2  
3 **Catalyst Preparation.** The functionalization of the silica was carried out by adding a desired  
4 amount of APTS to 30 mL of dry toluene containing 500 mg of silica. The resulting slurry was  
5 stirred for 12 h. The white solid was filtered and washed repeatedly with toluene. The white  
6 amine-functionalized silica ( $\text{SiO}_2\text{-NH}_2$ ) was dried in a vacuum oven (373 K and  $10^{-1}$  Torr) and  
7 used for further application. The presence of  $\text{-NH}_2$  functionalities on the  $\text{SiO}_2$  support surface  
8 was quantified by the colorimetric ninhydrin method.<sup>30</sup> PdAg-MnO<sub>x</sub>/N-SiO<sub>2</sub> catalyst was  
9 obtained by the conventional impregnation and subsequent reduction steps.<sup>31</sup> Typically, 5.0 mL  
10 aqueous solution containing Pd(NO<sub>3</sub>)<sub>2</sub>·2H<sub>2</sub>O (6.24 mg, 23.4 μmol Pd), AgNO<sub>3</sub> (0.80 mg, 4.7  
11 μmol Ag), Mn(NO<sub>3</sub>)<sub>2</sub>·4H<sub>2</sub>O (4.7 mg, 18.7 μmol Mn) and SiO<sub>2</sub>-NH<sub>2</sub> (100 mg, 100 μmol NH<sub>2</sub>) is  
12 mixed for 3 h. Then, the fresh 1.0 mL aqueous solution of NaBH<sub>4</sub> (28 mg, 0.7 mmol) was added  
13 to this mixture and the resulting solution was stirred for half an hour under ambient conditions.  
14 After centrifugation (6000 rpm, 5 min), copious washing with water (3 x 20 mL), filtration, and  
15 drying in oven at 373 K, PdAg-MnO<sub>x</sub>/N-SiO<sub>2</sub> catalyst was obtained as a dark gray powder.  
16  
17  
18  
19  
20  
21  
22  
23  
24  
25  
26  
27  
28  
29  
30  
31  
32  
33

34  
35 **Activity Measurements.** The catalytic activity of Pd-MnO<sub>x</sub>/SiO<sub>2</sub>-NH<sub>2</sub> in the additive-free FA  
36 dehydrogenation was determined by volumetric measurement of the rate of hydrogen evolution.  
37 The volume of released gas during the reaction was monitored using a gas burette through water  
38 displacement as described elsewhere.<sup>15-25</sup> Before starting the catalytic activity tests, a jacketed  
39 one-necked reaction flask (50.0 mL) containing a Teflon-coated stirring bar was placed on a  
40 magnetic stirrer (Heidolph MR-3004) whose temperature was adjusted by circulating water  
41 through its jacket from a constant temperature bath (Lab Companion RW-0525). In a typical  
42 catalytic activity test, PdAg-MnO<sub>x</sub>/N-SiO<sub>2</sub> catalyst was weighed and transferred into the reaction  
43 flask, and then 9.0 mL H<sub>2</sub>O was added into the reaction flask followed by rigorous stirring for 15  
44 min. to achieve thermal equilibrium. Next, 0.5 mL aqueous FA solution (0.1 mL FA + 0.4 mL  
45  
46  
47  
48  
49  
50  
51  
52  
53  
54  
55  
56  
57  
58  
59  
60

H<sub>2</sub>O) was added into the reaction flask via its septum using a 1.0 mL gastight syringe and the catalytic reaction was started (t = 0 min) by stirring the mixture at 600 rpm.

**Catalytic Selectivity.** The selectivity of PdAg-MnO<sub>x</sub>/N-SiO<sub>2</sub> catalyst in the decomposition of FA was investigated by GC analysis and NaOH-trap experiments. The gas generated over PdAg-MnO<sub>x</sub>/SiO<sub>2</sub>-NH<sub>2</sub> catalyzed dehydrogenation of aqueous FA solution (10.0 mL of 0.3 M) was collected in a GC analyzing balloon, which was then analyzed in GC by using pure CO, H<sub>2</sub> and CO<sub>2</sub> as reference gases. NaOH-trap experiments were performed to determine the molar ratio of CO<sub>2</sub> to H<sub>2</sub> in the product mixture generated during the PdAg-MnO<sub>x</sub>/SiO<sub>2</sub>-NH<sub>2</sub> catalyzed decomposition of aqueous FA solution (10 mL of 0.3 M).<sup>15-25</sup> In these experiments, the trap (10.0 M NaOH solution) was placed between the jacketed reactor and gas burette. The generated gas during the reaction was passed through the NaOH trap where CO<sub>2</sub> was captured (3). Next, the volume of the gas generated from the dehydrogenation of FA was monitored and compared to those without the trap experiment. We observed that the volume of the generated gas decreased by a factor of two in the presence of the NaOH trap. This result is indicative of the complete adsorption of CO<sub>2</sub> in NaOH solution (3) and the presence of equivalent molar amounts of CO<sub>2</sub> and H<sub>2</sub> (1.0:1.0) in the product mixture of the PdAg-MnO<sub>x</sub>/SiO<sub>2</sub>-NH<sub>2</sub> catalyzed additive-free FA dehydrogenation.



**Catalytic Stability.** The recyclability of PdAg-MnO<sub>x</sub>/N-SiO<sub>2</sub> in the additive-free dehydrogenation of FA was determined by a series of experiments started with a 10.0 mL aqueous FA solution (0.1 mL FA + 9.9 mL H<sub>2</sub>O) at 298 K. Immediately after the achievement of complete conversion, another equivalent amount of FA was added to the reaction mixture,

1  
2  
3 leading further hydrogen evolution. The same procedure was repeated up to the 5<sup>th</sup> subsequent  
4 catalytic recycle. In the reusability experiments the catalyst was isolated from the reaction  
5 solution by centrifugation after the first catalytic run and washed with excess water and dried at  
6 373 K. The dried catalyst was weighed and reused in the catalytic dehydrogenation of a 10.0 mL  
7 aqueous FA solution (0.1 mL FA + 9.9 mL H<sub>2</sub>O) at 298 K. This identical catalyst was isolated  
8 and reused up to 5 consecutive catalytic cycles.  
9  
10  
11  
12  
13  
14  
15  
16  
17  
18

19 **Cyclic Voltammetry (CV) Measurements.** CV measurements were carried out in a  
20 conventional three-electrode cell with a Pt wire as the counter electrode and Ag/AgCl as the  
21 reference electrode with a CHI 660E potentiostat. The working electrode was a glassy carbon  
22 disk having a diameter of 3.0 mm held in a Teflon cylindrical housing. Before the CV  
23 measurements, the surface of the glassy carbon electrode was polished with alumina to prepare  
24 the surface of the electrode for the catalyst deposition process. For the electrode preparation,  
25 typically 7-9 mg of catalyst was dispersed in a 1.0 mL 5% Nafion® medium (Aldrich) to obtain  
26 a catalyst suspension. Then, 6.0  $\mu\text{L}$  of this suspension was drop-cast on the surface of the glassy  
27 carbon electrode. Then, the electrode was dried at room temperature to remove the solvent. CV's  
28 were recorded between -0.23 V and 1.0 V with a scan rate of 10 mV s<sup>-1</sup> in the presence of 0.5 M  
29 H<sub>2</sub>SO<sub>4</sub> and 1.0 M HCOOH. Prior to the CV experiments, the electrolyte was saturated with N<sub>2</sub>  
30 and the electrode surface was activated via 0.5 M H<sub>2</sub>SO<sub>4</sub>.  
31  
32  
33  
34  
35  
36  
37  
38  
39  
40  
41  
42  
43  
44  
45  
46  
47

48 **Linear Sweep Voltammetry (LSV) Measurements.** Linear sweep voltammetry (LSV)  
49 technique was employed to investigate the CO adsorption on the PdAg/SiO<sub>2</sub>-NH<sub>2</sub> and PdAg-  
50 MnO<sub>x</sub>/SiO<sub>2</sub>-NH<sub>2</sub> catalyst surface, which can poison the surface during the decomposition of  
51 formic acid.<sup>32,33</sup> Before the LSV measurements, catalysts were exposed to a pretreatment process,  
52  
53  
54  
55  
56  
57  
58  
59  
60

1  
2  
3 where the catalyst surfaces were maintained at a constant potential of 0.0 V for 180 s. After the  
4 pretreatment, LSV measurements were carried out to determine the activity of the pretreated  
5 surfaces in the electrocatalytic oxidation of FA. These measurements were conducted within the  
6 bias range of -0.2 V to 0.9 V in a solution containing 0.5 M H<sub>2</sub>SO<sub>4</sub> and 1.0 M HCOOH using a  
7  
8  
9  
10  
11  
12  
13 10 mV s<sup>-1</sup> scan rate.

14  
15  
16 **CO-Stripping Voltammetry Measurements.** 5 mg catalyst sample was dispersed in 1.0 mL  
17 5% Nafion® solution (Aldrich) to obtain a catalyst suspension. Next, 5.0 μL of this suspension  
18 was drop-cast on the surface of the glassy carbon electrode. All electrolyte solutions were  
19 deaerated with high-purity nitrogen for 30 min prior to the measurements. For CO stripping  
20 voltammetry, 0.5 M H<sub>2</sub>SO<sub>4</sub> solution was first bubbled with pure nitrogen for 30 min in order to  
21 remove the dissolved oxygen. CO was then purged into the solution for 20 min to allow  
22 saturation of the electrocatalyst surface with adsorbed CO, while maintaining a constant potential  
23 of 0.0 V. Excess CO was then purged with nitrogen for 30 min.

24  
25  
26  
27  
28  
29  
30  
31  
32  
33  
34  
35  
36 **In-Situ FTIR Spectroscopic Analyses.** Detailed description of the instrumentation used in  
37 the currently presented in-situ FTIR experiments can be found elsewhere.<sup>34</sup> Briefly, *in-situ* FTIR  
38 spectroscopic measurements were performed in transmission mode using a Bruker Tensor 27  
39 FTIR spectrometer which was modified to house a batch-type custom-made in-situ spectroscopic  
40 reactor. All catalysts were initially cleaned by annealing under vacuum (< 1x 10<sup>-3</sup> Torr) at 400 K  
41 for 2 h. This process is needed to thermally remove the adsorbed water on the material surfaces  
42 and obtain materials that are relatively more transparent to the IR beam. CO adsorption  
43 (poisoning) experiments were performed by introducing 20.0 Torr of CO (>99.995% purity, Air  
44 Products) for 10 min at 323 K followed by evacuation at ~10<sup>-3</sup> Torr. FA adsorption was  
45  
46  
47  
48  
49  
50  
51  
52  
53  
54  
55  
56  
57  
58  
59  
60

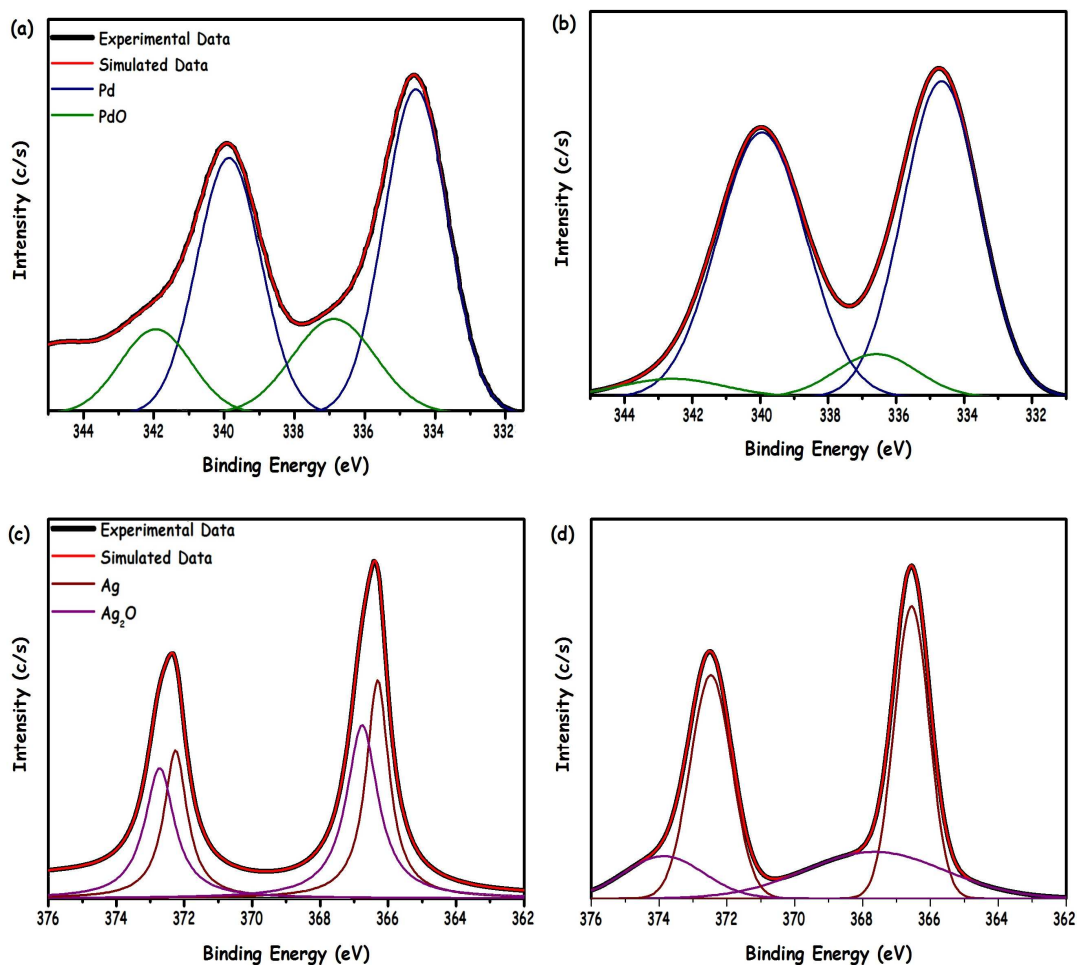
1  
2  
3 performed on CO pre-adsorbed (*i.e.* poisoned) catalyst surfaces where the FTIR spectra for the  
4 CO-poisoned surfaces were used as the corresponding background spectra. In these set of  
5 experiments, after 20.0 Torr of CO adsorption at 323 K for 10 min, 5.0 Torr of FA was dosed on  
6 the poisoned catalysts for 5 minutes. Next, the reactor was evacuated ( $P < 10^{-2}$  Torr) and FTIR  
7 spectra were acquired. All FTIR spectra in this study were collected at 323 K.  
8  
9  
10  
11  
12  
13  
14  
15

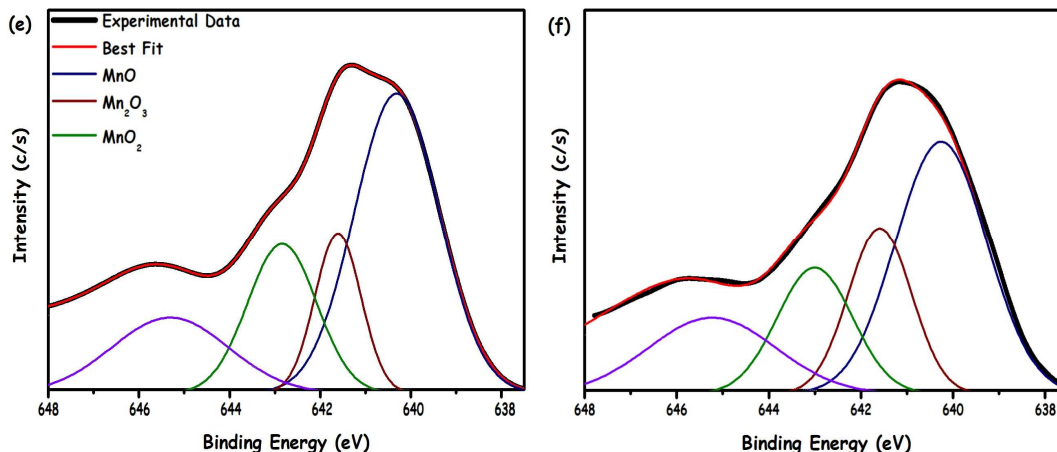
## 16 RESULTS AND DISCUSSION

17  
18  
19 **Catalyst Preparation and Characterization.** PdAg-MnO<sub>x</sub>/N-SiO<sub>2</sub> catalyst can simply and  
20 reproducibly be prepared by following the procedure comprising of the conventional  
21 impregnation<sup>31</sup> of Pd<sup>2+</sup>, Ag<sup>+</sup> and Mn<sup>2+</sup> onto amine-functionalized silica and their borohydride  
22 reduction at room temperature. After centrifugation, copious washing with water, PdAg-  
23 MnO<sub>x</sub>/N-SiO<sub>2</sub> catalyst was isolated as gray powder and characterized by multi pronged  
24 techniques. The elemental composition of the as-prepared PdAg-MnO<sub>x</sub>/SiO<sub>2</sub>-NH<sub>2</sub> catalyst was  
25 found to be Pd<sub>0.44</sub>Ag<sub>0.19</sub>Mn<sub>0.37</sub> (*i.e.* 1.27 wt% Pd, 0.57 wt% Ag, and 0.54 wt% Mn;  
26 corresponding to relative molar amounts of 11.9 μmol Pd, 5.3 μmol Ag, 9.8 μmol Mn and 0.98  
27 mmol NH<sub>2</sub>/g SiO<sub>2</sub>) by ICP-OES analyses and ninhydrin method.<sup>30</sup> The survey XPS spectrum of  
28 PdAg-MnO<sub>x</sub>/SiO<sub>2</sub>-NH<sub>2</sub> catalyst (Figure S1) shows the existence of Pd, Ag and Mn with the  
29 elements of support material (Si, O, C and N). Pd 3d, Ag 3d and Mn 2p XPS spectra of the  
30 PdAg-MnO<sub>x</sub>/SiO<sub>2</sub>-NH<sub>2</sub> catalyst together with their deconvoluted chemical states are given in  
31 Figure 1 (a), (c) and (e). These results reveal the presence of metallic (*i.e.* Pd<sup>0</sup> with Pd 3d<sub>5/2</sub> at  
32 334.5 eV and Pd 3d<sub>3/2</sub> at 339.8 eV), as well as oxidic (*i.e.* Pd<sup>2+</sup> with Pd 3d<sub>5/2</sub> at 336.9 eV and Pd  
33 3d<sub>3/2</sub> at 341.9 eV) Pd states.<sup>35</sup> Ag was also found be in both metallic (*i.e.* Ag<sup>0</sup> with Ag 3d<sub>5/2</sub> 366.8  
34 eV and Ag 3d<sub>3/2</sub> 372.8 eV), and oxidic (*i.e.* Ag<sup>+</sup> with Ag 3d<sub>5/2</sub> 366.5 eV; Ag 3d<sub>3/2</sub> 372.9 eV)  
35  
36  
37  
38  
39  
40  
41  
42  
43  
44  
45  
46  
47  
48  
49  
50  
51  
52  
53  
54  
55  
56  
57  
58  
59  
60

1  
2  
3  
4  
5  
6  
7  
8  
9  
10  
11  
12  
13  
14  
15  
16  
17  
18  
19  
20  
21  
22  
23  
24  
25  
26  
27  
28  
29  
30  
31  
32  
33  
34  
35  
36  
37  
38  
39  
40  
41  
42  
43  
44  
45  
46  
47  
48  
49  
50  
51  
52  
53  
54  
55  
56  
57  
58  
59  
60

states.<sup>36</sup> On the other hand, Mn was found to exist in the form of  $\text{Mn}^{2+}$  (Mn 2p<sub>3/2</sub> at 640.3 eV),  $\text{Mn}^{3+}$  (Mn 2p<sub>3/2</sub> at 641.6 eV) and  $\text{Mn}^{4+}$  (Mn 2p<sub>3/2</sub> at 642.8 eV)<sup>37,38</sup> exhibiting an additional high-binding energy shake-up peak feature at 645.5 eV.<sup>38</sup> XPS spectra presented in Figure 1 (b) and (d) suggest that after  $\text{Ar}^+(\text{g})$  sputtering for 5 min, XPS features associated with  $\text{Pd}^{2+}$  and  $\text{Ag}^+$  could be removed where  $\text{Pd}^0$  and  $\text{Ag}^0$  exist as the predominant features. However, oxidic forms of Mn continue to exist even after  $\text{Ar}^+(\text{g})$  sputtering (Figure 1(f)) without any major alteration. Existence of oxidic states of Mn is not unexpected as the high oxophilicity of Mn makes  $\text{Mn}^0$  NPs highly reactive upon exposure to air leading to the generation of various forms of  $\text{MnO}_x$  states with high stability.<sup>39,40</sup>

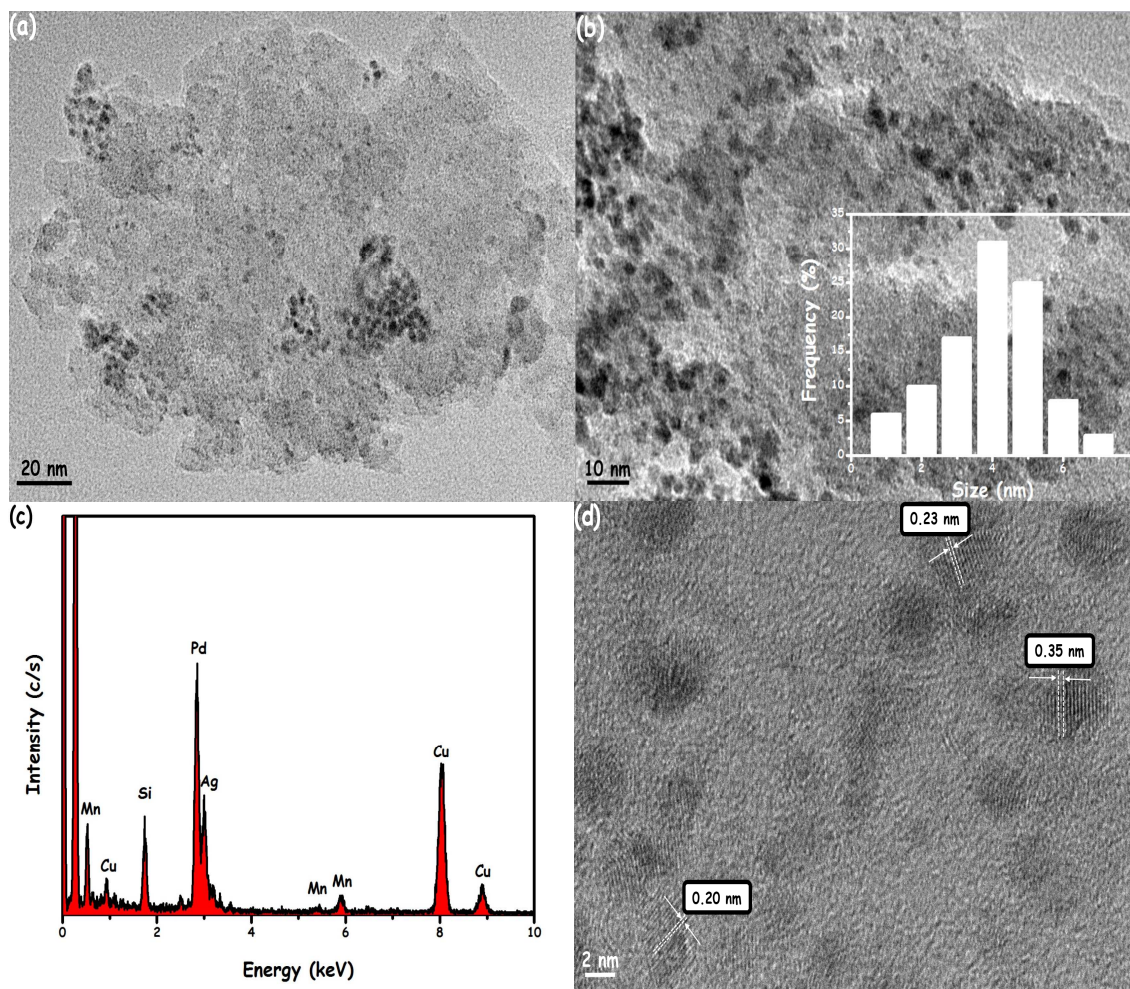




**Figure 1.** Pd 3d XP spectra (a) before, (b) after (5 min.) Ar<sup>+</sup>(g) sputtering, Ag 3d XPS spectra (c) before, (d) after (5 min.) Ar<sup>+</sup>(g) sputtering, Mn 2p XP spectra (e) before, (f) after (5 min.) Ar<sup>+</sup>(g) sputtering for PdAg-MnO<sub>x</sub>/N-SiO<sub>2</sub> catalyst.

TEM, HRTEM, STEM-EDX and HAADF-STEM-mapping investigations were performed to examine the size, morphology and the composition of the PdAg-MnO<sub>x</sub>/N-SiO<sub>2</sub> catalyst. TEM images of PdAg-MnO<sub>x</sub>/N-SiO<sub>2</sub> given in Figure 2 (a) and (b) reveal the presence of PdAg and MnO<sub>x</sub> nanoparticles (for comparison TEM image of metal-free see N-SiO<sub>2</sub> is given in Figure S2). The mean particle size for the images given in Figure 2 (a-b) was found to be ca. 6.4 nm using the NIH image program,<sup>41</sup> which included the particle size analysis for > 100 non-touching particles (Figure 2 (b) inset). STEM-EDX analysis of a large number of different domains on the PdAg-MnO<sub>x</sub>/N-SiO<sub>2</sub> surface confirmed the presence of Pd, Ag and Mn in the analyzed regions (Figure 2 (c)). HRTEM image of PdAg-MnO<sub>x</sub>/N-SiO<sub>2</sub> is given in Figure 2(d) displaying the highly crystalline nature of the NPs on the PdAg-MnO<sub>x</sub>/N-SiO<sub>2</sub> surface. Three different crystalline fringe distances (0.20, 0.23 and 0.35 nm) were measured for three individual NPs. The fringe distances of 0.20 and 0.35 nm can be assigned to MnO<sub>2</sub><sup>42</sup> and Mn<sub>2</sub>O<sub>3</sub><sup>43</sup> phases, respectively. On the other hand, the fringe distance of 0.23 nm, which is between the (111) lattice spacing of face-centered cubic (*fcc*) Ag (0.24 nm) and *fcc* Pd (0.22 nm), can be attributed

1  
2  
3  
4 to a PdAg alloy structure. In addition to that, XRD pattern of the as-synthesized catalyst (Figure  
5 S3) exhibits a diffraction peak located between the characteristic Pd (111) and Ag (111)  
6 diffraction features. DR-UV-Vis spectrum taken from solid powders of PdAg-MnO<sub>x</sub>/N-SiO<sub>2</sub>  
7  
8 diffraction features. DR-UV-Vis spectrum taken from solid powders of PdAg-MnO<sub>x</sub>/N-SiO<sub>2</sub>  
9  
10 (Figure S4), shows a very weak surface plasmon resonance (SPR) feature, whereas Ag/SiO<sub>2</sub>-NH<sub>2</sub>  
11  
12 and Ag-MnO<sub>x</sub>/N-SiO<sub>2</sub> samples reveal much stronger SPR bands at ca. 440 nm. It is worth  
13  
14 mentioning that, quenching of the SPR bands due to alloying was also observed for oleylamine-  
15  
16 stabilized PdAg alloy NPs.<sup>23</sup>  
17  
18  
19  
20



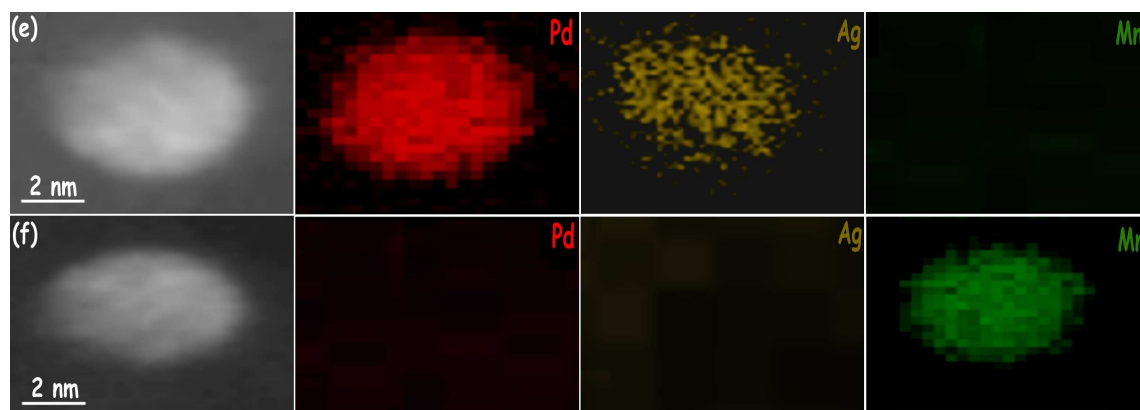
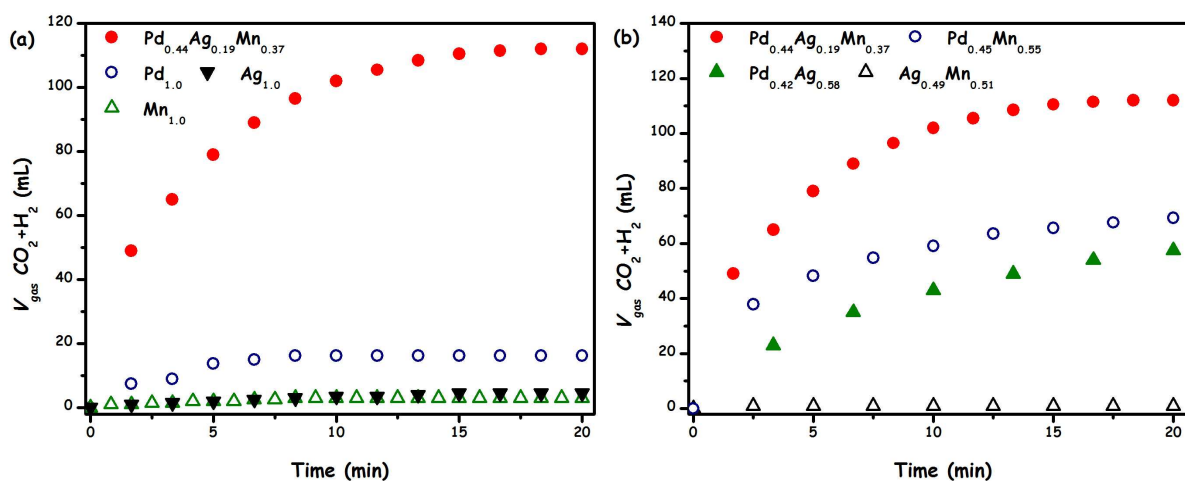


**Figure 2.** (a-b) TEM images and particle size distribution (inset in (b)), (c) TEM-EDX spectrum, (d) HRTEM image of the PdAg-MnO<sub>x</sub>/N-SiO<sub>2</sub> catalyst; (e) and (f) HAADF-STEM images, HAADF-STEM elemental mapping for Pd, Ag and Mn of the PdAg-MnO<sub>x</sub>/N-SiO<sub>2</sub> catalyst.

The compositional analyses of the PdAg-MnO<sub>x</sub>/N-SiO<sub>2</sub> catalyst were also performed by detailed HAADF-STEM measurements. Figure 2 also presents HAADF-STEM images (Figure 2 (e) and (f)) as well as elemental mapping analysis of Pd, Ag and Mn for two independent particles existing on the PdAg-MnO<sub>x</sub>/N-SiO<sub>2</sub> catalyst surface. While HAADF-STEM-elemental mapping suggests the existence of a PdAg alloy for the first particle in the absence of any Mn signal, the second particle reveals the exclusive presence of Mn lacking appreciable Pd or Ag signals. These results support the presence of individual PdAg alloy NPs that are separate from the MnO<sub>x</sub> NPs on the N-SiO<sub>2</sub> support surface. On the other hand, as it is difficult to establish a true statistical analysis using microscopic probes, presence of a minor amount of overlapping domains of PdAg and MnO<sub>x</sub> cannot be excluded.

**Catalytic Performance Results.** For a comprehensive elucidation of the catalytic activity of the PdAg-MnO<sub>x</sub>/N-SiO<sub>2</sub> catalytic architecture towards additive-free dehydrogenation of FA; we followed a systematic approach, where the individual catalytic performance of each structural subcomponent (*i.e.* single-component samples such as Pd<sub>1.0</sub>/N-SiO<sub>2</sub>, Ag<sub>1.0</sub>/N-SiO<sub>2</sub>, Mn<sub>1.0</sub>/N-SiO<sub>2</sub>) was studied (Figure 3 (a)-(d)) in addition to binary combinations of these subcomponents

(i.e.  $\text{Pd}_{0.45}\text{-Mn}_{0.55}/\text{N-SiO}_2$ ,  $\text{Pd}_{0.42}\text{Ag}_{0.58}/\text{N-SiO}_2$ ,  $\text{Ag}_{0.49}\text{-Mn}_{0.51}/\text{N-SiO}_2$ ) as well as their ternary counterparts (i.e.  $\text{Pd}_{0.40}\text{Ag}_{0.12}\text{-Mn}_{0.48}/\text{N-SiO}_2$ ,  $\text{Pd}_{0.44}\text{Ag}_{0.19}\text{-Mn}_{0.37}/\text{N-SiO}_2$ ,  $\text{Pd}_{0.48}\text{Ag}_{0.27}\text{-Mn}_{0.25}/\text{N-SiO}_2$ ,  $\text{Pd}_{0.55}\text{Ag}_{0.35}\text{-Mn}_{0.10}/\text{N-SiO}_2$ ). Evidently,  $\text{Pd}_{0.44}\text{Ag}_{0.19}\text{-Mn}_{0.37}/\text{N-SiO}_2$  catalyst provides the best activity compared to all other investigated catalysts. Comparison of Figure 3 (a) and Figure 3 (b) strongly implies that Pd has a critical role in the FA decomposition, as the catalytic activity is completely lost in the absence of Pd (e.g.  $\text{Ag}_{1.0}/\text{N-SiO}_2$ ,  $\text{Mn}_{1.0}/\text{N-SiO}_2$ , and  $\text{Ag}_{0.49}\text{-Mn}_{0.51}/\text{N-SiO}_2$ ). On the other hand, the initially high activity of the single-component  $\text{Pd}_{1.0}/\text{N-SiO}_2$  catalyst is not sustainable as the active sites can readily be deactivated due to the generation of a poisonous byproduct (i.e. CO), demonstrating the paramount challenges associated with the use of a single-component catalytic architecture in formic acid decomposition lacking additional promoters such as Ag and Mn.<sup>4,5</sup>



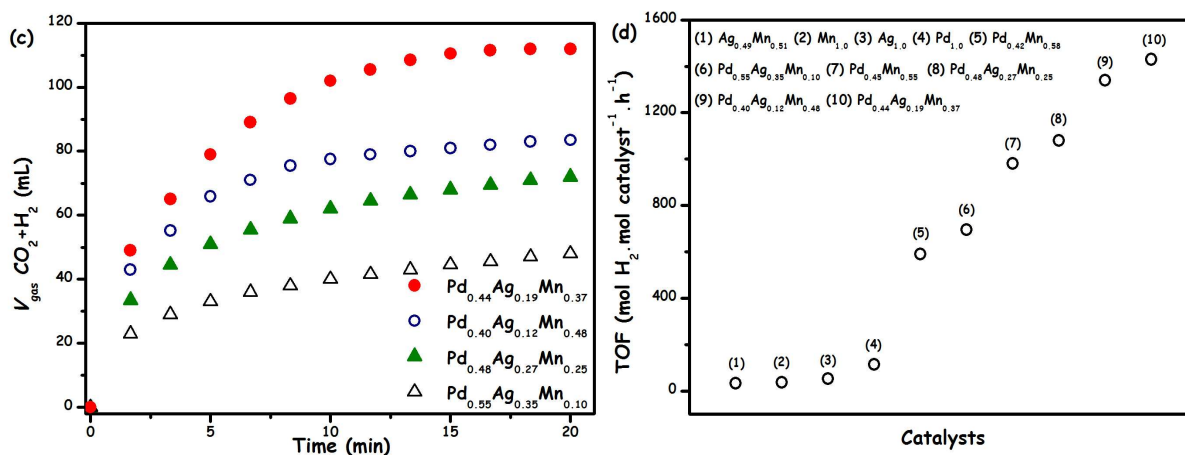


**Figure 3.** The volume of generated gas ( $\text{CO}_2 + \text{H}_2$ ) (mL) versus time (min.) graphs of (a) monometallic, (b) bimetallic, (c) trimetallic catalysts, (d) TOF values versus catalysts in different [Pd]:[Ag]:[Mn] ratios for the additive-free FA dehydrogenation (0.25 M in 10.0 mL  $\text{H}_2\text{O}$ ) at 313 K.

Although, binary systems such as  $\text{Pd}_{0.45}\text{-Mn}_{0.55}/\text{N-SiO}_2$  and  $\text{Pd}_{0.42}\text{Ag}_{0.58}/\text{N-SiO}_2$  show better activities than  $\text{Pd}_{1.0}/\text{N-SiO}_2$ , their performances are still far inferior to the ternary  $\text{Pd}_{0.44}\text{Ag}_{0.19}\text{-Mn}_{0.37}/\text{N-SiO}_2$  system (Figure 3). Morphological investigation by TEM (Figure S5) reveals that NPs of the single-component and binary systems have smaller particle sizes with respect to the ternary  $\text{Pd}_{0.44}\text{Ag}_{0.19}\text{-Mn}_{0.37}/\text{N-SiO}_2$  system. The uniqueness of the  $\text{Pd}_{0.44}\text{Ag}_{0.19}\text{-Mn}_{0.37}/\text{N-SiO}_2$  catalyst structure was further supported by two control experiments where physical mixture of (i)  $\text{Pd}/\text{N-SiO}_2$ ,  $\text{Ag}/\text{N-SiO}_2$ ,  $\text{Mn}/\text{N-SiO}_2$  (with a Pd:Ag:Mn molar ratio of 0.45:0.21:0.34) and (ii)  $\text{Pd}_{0.41}\text{Ag}_{0.59}/\text{N-SiO}_2$  and  $\text{Mn}_{0.37}/\text{N-SiO}_2$  exhibited a lower activity than that of  $\text{Pd}_{0.44}\text{Ag}_{0.19}\text{-Mn}_{0.37}/\text{N-SiO}_2$  catalyst in FA dehydrogenation in the absence of additives under identical conditions (Figure S6). These control experiments demonstrate a proximity requirement associated with the synergistic structural components of the  $\text{Pd}_{0.44}\text{Ag}_{0.19}\text{-Mn}_{0.37}/\text{N-SiO}_2$  catalyst, which interact in an efficient manner during additive-free dehydrogenation of FA. The generated gas obtained via  $\text{Pd}_{0.44}\text{Ag}_{0.19}\text{-Mn}_{0.37}/\text{N-SiO}_2$ -catalyzed FA dehydrogenation was analyzed by gas

1  
2  
3 chromatography (GC) in the presence or absence of the NaOH trap (Figure S7). These  
4  
5 experiments revealed that the generated gas is a mixture of H<sub>2</sub> and CO<sub>2</sub> with a H<sub>2</sub>:CO<sub>2</sub> molar  
6  
7 ratio of 1.0:1.0 where CO was below the detection limit (*i.e.* < 10 ppm). In other words, these  
8  
9 experiments point to the important fact that CO-free H<sub>2</sub> generation can be achieved in the  
10  
11 absence of additives from an aqueous FA solution for fuel cell applications<sup>6</sup> at ambient  
12  
13 conditions by utilizing a Pd<sub>0.44</sub>Ag<sub>0.19</sub>-Mn<sub>0.37</sub>/N-SiO<sub>2</sub> catalyst.

14  
15  
16  
17  
18  
19 Figure 4 (a) shows the volume of generated gas (CO<sub>2</sub> + H<sub>2</sub>) versus the reaction time for  
20  
21 Pd<sub>0.44</sub>Ag<sub>0.19</sub>-Mn<sub>0.37</sub>/N-SiO<sub>2</sub> catalyzed additive-free FA dehydrogenation at different temperatures.  
22  
23 It is apparent that Pd<sub>0.44</sub>Ag<sub>0.19</sub>-Mn<sub>0.37</sub>/N-SiO<sub>2</sub> catalyst provides *initial* TOF values of 330, 530,  
24  
25 700, 1430 mol H<sub>2</sub>.mol catalyst<sup>-1</sup>.h<sup>-1</sup> at 298, 303, 308 and 313 K, respectively (see Supporting  
26  
27 Information for details of the calculation of initial TOF values). The *initial* TOF value of 330  
28  
29 mol H<sub>2</sub>.mol catalyst<sup>-1</sup>.h<sup>-1</sup> (corresponding to 750 mol H<sub>2</sub>.mol Pd<sup>-1</sup>.h<sup>-1</sup>; 524 mol H<sub>2</sub>.mol (Pd+Ag)  
30  
31 <sup>-1</sup>.h<sup>-1</sup> assuming that the active sites are only provided by Pd or PdAg NPs; respectively) measured  
32  
33 at 298 K is one of the most remarkable TOF values reported for FA dehydrogenation at room  
34  
35 temperature using a heterogeneous catalyst without utilizing any additives (Table 1).  
36  
37  
38  
39  
40

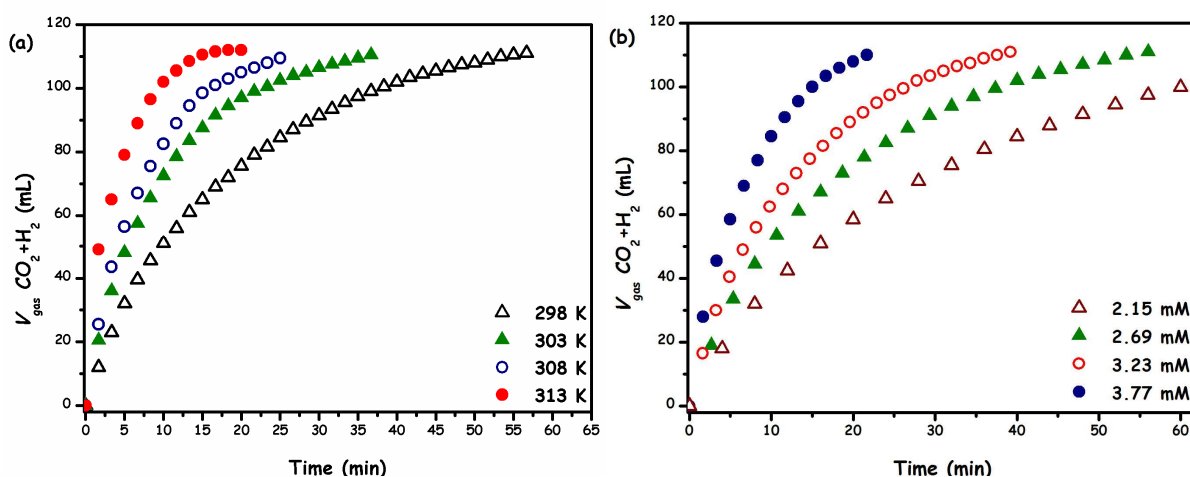


**Figure 4.** (a) The volume of the generated gas versus time plots for Pd<sub>0.44</sub>Ag<sub>0.19</sub>-Mn<sub>0.37</sub>/N-SiO<sub>2</sub> (2.69 mM) catalyzed additive-free dehydrogenation of FA (0.25 M FA in 10.0 mL H<sub>2</sub>O) at different temperatures, (b) analogous data for 0.25 M FA in 10.0 mL H<sub>2</sub>O at 298 K corresponding to varying catalyst (Pd<sub>0.44</sub>Ag<sub>0.19</sub>-Mn<sub>0.37</sub>/N-SiO<sub>2</sub>) concentrations.

More importantly, FA dehydrogenation can be completed in less than an hour with > 99 % conversion. The values of observed rate constants  $k_{\text{obs}}$  determined from the linear portions of the volume of generated gas (CO<sub>2</sub> + H<sub>2</sub>) versus reaction time plots at four different temperatures are used to obtain Arrhenius and Eyring plots (Figure S8 and Figure S9) to calculate activation parameters. Using these plots, apparent activation energy ( $E_a$ ), apparent activation enthalpy ( $\Delta H_a^\ddagger$ ) and apparent activation entropy ( $\Delta S_a^\ddagger$ ) values were calculated to be 72.4 kJ/mol, 69.1 kJ/mol and 37.5 J/mol.K, respectively. The positive magnitude of the apparent activation entropy implies the presence of a dissociative mechanism in the transition state (*vide infra*).<sup>44</sup>

**Table 1.** Comparison of the catalytic performance data for the currently studied Pd-MnO<sub>x</sub>/SiO<sub>2</sub>-NH<sub>2</sub> catalyst with the prior best heterogeneous catalyst systems reported for the dehydrogenation FA in the absence of any additives at low temperatures

Catalyst	Temp. (K)	Conv. (%)	Activity (h <sup>-1</sup> ) <sup>a</sup>	Ref.
Ag@Pd	293	36	63	18
AgPd	293	10	72	18
Au@Pd	298	89	98	19
CoAuPd/C	298	91	37	20
CoAuPd/GO	298	51	45	21
CoAuPd/DNA	298	96	85	21
AuPd	298	28	41	22
AgPd	298	52	180	23

Pd-MnO <sub>x</sub>	298	63	150	24
PdAu-MnO <sub>x</sub> /MOF-Graphene	298	94	382 <sup>b</sup>	25
PdAuCr/N-SiO <sub>2</sub>	298	99	730	26
PdAg-MnO <sub>x</sub> /N-SiO <sub>2</sub>	298	99	524 <sup>c</sup>	this study
PdAg-MnO <sub>x</sub> /N-SiO <sub>2</sub>	298	99	330	this study

<sup>a</sup> TOF = mol H<sub>2</sub>/mol total metal × h and these TOF values are not corrected for the number of exposed surface atoms; that is, the values given are lower limits; <sup>b</sup> Based on Au and Pd atoms; <sup>c</sup> Based on Ag and Pd atoms

In addition to the effect of temperature, we also investigated the influence of the catalyst concentration on the rate of the additive-free dehydrogenation of FA by performing the catalytic reaction starting with different Pd<sub>0.44</sub>Ag<sub>0.19</sub>-Mn<sub>0.37</sub>/N-SiO<sub>2</sub> concentrations at 298 K (Figure 4 (b)). The reaction rates for each catalyst concentration were calculated from the linear portion of each plot given in Figure 4(b). The logarithmic plot of the hydrogen generation rate versus catalyst concentration (Figure S10) gives a line with a slope of 1.18, which indicates that Pd<sub>0.44</sub>Ag<sub>0.19</sub>-Mn<sub>0.37</sub>/N-SiO<sub>2</sub> catalyzed additive-free FA dehydrogenation, is close to first-order with respect to the catalyst concentration within the investigated concentration window.

The catalytic stability of the PdAg-MnO<sub>x</sub>/N-SiO<sub>2</sub> catalyst in the additive-free dehydrogenation of FA was investigated by performing recycling and reusability experiments. When all of FA was converted to CO<sub>2</sub> and H<sub>2</sub> in a particular cycle, more FA was added into the solution and the reaction was continued up to five consecutive catalytic cycles. It was found that PdAg-MnO<sub>x</sub>/N-SiO<sub>2</sub> catalyst (*i.e.* Pd<sub>0.44</sub>Ag<sub>0.19</sub>-Mn<sub>0.37</sub>/N-SiO<sub>2</sub>) retains 86 % of its initial activity and provides 98 % of conversion without CO generation after the 5<sup>th</sup> consecutive cycle (Figure 5(a)). Ease of isolation and reusability characteristics of PdAg-MnO<sub>x</sub>/N-SiO<sub>2</sub> were also tested in the FA dehydrogenation under identical conditions. After the complete dehydrogenation of FA,

PdAg-MnO<sub>x</sub>/N-SiO<sub>2</sub> catalyst was isolated as a dark gray powder and bottled under nitrogen atmosphere. Then, the isolated PdAg-MnO<sub>x</sub>/N-SiO<sub>2</sub> catalyst was re-dispersed in the aqueous FA solution. This re-dispersed catalyst preserved 80 % of its initial activity with a 95 % conversion of FA to CO<sub>2</sub> and H<sub>2</sub> even after the 5<sup>th</sup> catalytic reuse (Figure 5(c)).

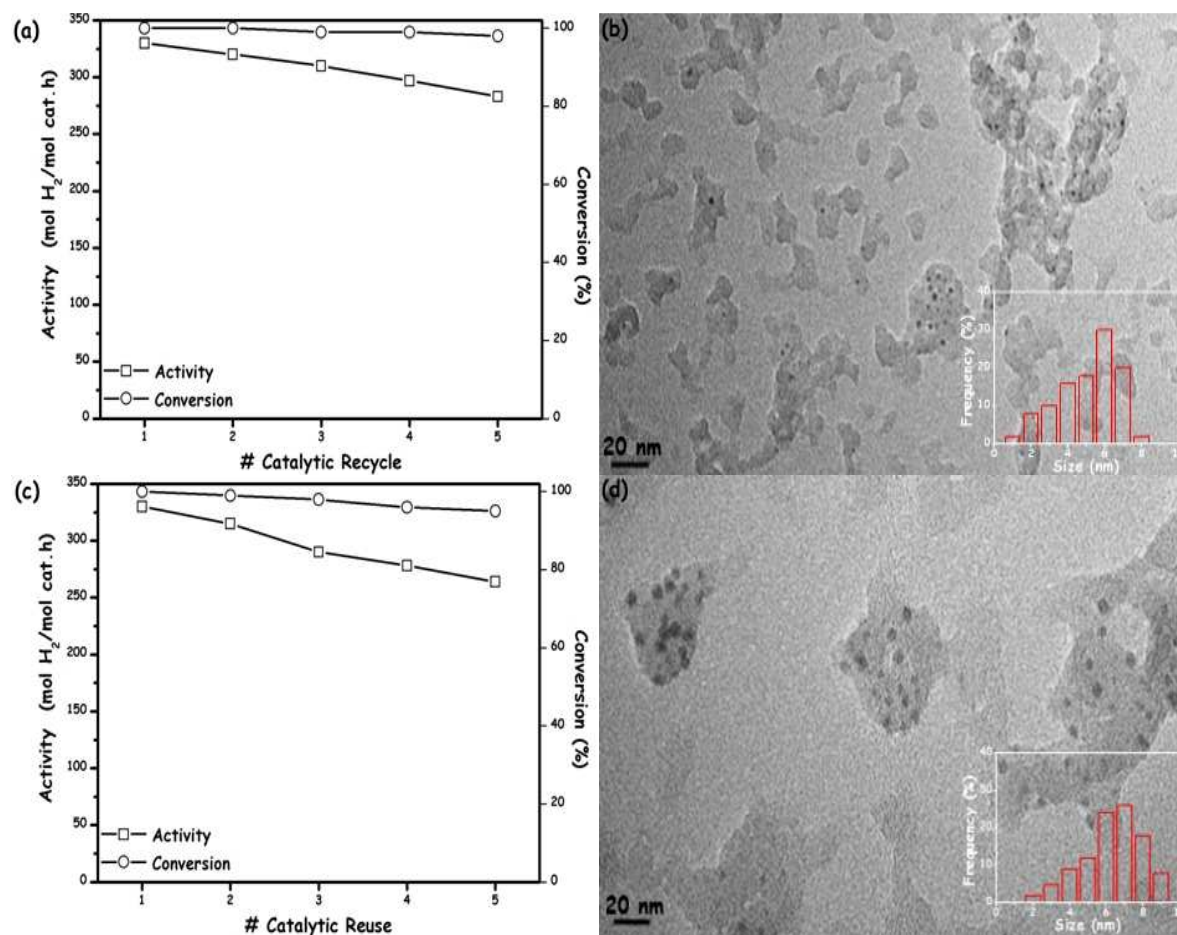


**Figure 5.** (a) Activity and conversion versus number of catalytic cycles for Pd<sub>0.44</sub>Ag<sub>0.19</sub>-Mn<sub>0.37</sub>/N-SiO<sub>2</sub>-catalyzed FA dehydrogenation in the absence of additives at 298 K, (b) TEM image of Pd<sub>0.44</sub>Ag<sub>0.19</sub>-Mn<sub>0.37</sub>/N-SiO<sub>2</sub> recovered after the 5<sup>th</sup> catalytic recycle (inset shows the particle size distribution of PdAg-MnO<sub>x</sub> NPs), (c) Activity and conversion versus number of catalytic reuse at 298 K, (d) TEM image of Pd<sub>0.44</sub>Ag<sub>0.19</sub>-Mn<sub>0.37</sub>/N-SiO<sub>2</sub> catalyst recovered after the 5<sup>th</sup> catalytic reuse with PdAg-MnO<sub>x</sub> NPs size distribution (inset).

1  
2  
3  
4  
5  
6  
7  
8  
9  
10  
11  
12  
13  
14  
15  
16  
17  
18  
19  
20  
21  
22  
23  
24  
25  
26  
27  
28  
29  
30  
31  
32  
33  
34  
35  
36  
37  
38  
39  
40  
41  
42  
43  
44  
45  
46  
47  
48  
49  
50  
51  
52  
53  
54  
55  
56  
57  
58  
59  
60

TEM analysis of PdAg-MnO<sub>x</sub>/N-SiO<sub>2</sub> samples recovered after 5<sup>th</sup> consecutive catalytic run of the recycling and reusability experiments (Figure 5 (b) and Figure 5 (d)) show a slight increase in the average particle size of PdAg-MnO<sub>x</sub> NPs (6.8 and 7.9 nm, respectively) consistent with the minor decrease in the activity at the end of these experiments. Moreover, ICP-OES and elemental analysis of used and isolated PdAg-MnO<sub>x</sub>/N-SiO<sub>2</sub> catalyst samples and reaction solutions indicated that (i) metal and -NH<sub>2</sub> contents of the catalysts remained intact after use and (ii) leaching of metals and/or surface grafted amines into the reaction solution was not observed. Additionally, removing the PdAg-MnO<sub>x</sub>/N-SiO<sub>2</sub> catalyst from the reaction solution can completely stop the dehydrogenation of FA. These results are indicative of the high stability of PdAg-MnO<sub>x</sub> NPs against agglomeration and leaching throughout the catalytic runs.

**Effect of Surface Grafted Amine Groups on the Catalytic Activity.** In a series of additional experiments, we also compared the catalytic activities of PdAg-MnO<sub>x</sub>/N-SiO<sub>2</sub>, which were functionalized with different amounts of amine groups, in the additive-free dehydrogenation of FA under identical reaction conditions in order to understand the effect of the surface-grafted amine functionalities on the catalytic reactivity (Figure S11). We found that amine-free SiO<sub>2</sub> supported PdAg-MnO<sub>x</sub> catalyst (Pd<sub>0.41</sub>Ag<sub>0.20</sub>-Mn<sub>0.39</sub>/SiO<sub>2</sub>) provides the lowest gas generation rate (6.35 mL/min) and the catalytically optimum amine loading is 0.98 mmol NH<sub>2</sub>/g, where the maximum gas generation rate can be achieved by Pd<sub>0.44</sub>Ag<sub>0.19</sub>-Mn<sub>0.37</sub> NPs (30.8 mL/min).

The limited reactivity of Pd<sub>0.41</sub>Ag<sub>0.20</sub>-Mn<sub>0.39</sub> NPs supported on amine-free SiO<sub>2</sub> can be explained by the absence of -NH<sub>2</sub> functionalities on the support material, which may have a direct impact on the FA adsorption/storage process as well as the nucleation and growth of the

1  
2  
3 PdAg and MnO<sub>x</sub> NPs on the support surface (Figure S12). In a recent study Yamashita *et al.*<sup>45</sup>  
4  
5 reported that a resin bearing -N(CH<sub>3</sub>)<sub>2</sub> acted as a significantly more efficient organic support  
6  
7 material in the catalytic decomposition of FA than those bearing -SO<sub>3</sub>H, -COOH and -OH for Pd  
8  
9 or Ag@Pd NPs. Their mechanistic studies revealed that O-H bond cleavage in FA is facilitated  
10  
11 by the -N(CH<sub>3</sub>)<sub>2</sub> functionalities leading to the formation of metal-bound formate species along  
12  
13 with a -[N(CH<sub>3</sub>)<sub>2</sub>H]<sup>+</sup> species, followed by the dehydrogenation of the metal-bound formate,  
14  
15 producing H<sub>2</sub> and CO<sub>2</sub>. In the light of these results, it is reasonable to propose that the existence  
16  
17 of surface-grafted amine functionalities in the currently exploited support material efficiently  
18  
19 acts as a proton scavenger providing a basic environment around the PdAg-MnO<sub>x</sub> NPs. It is  
20  
21 feasible that amine-grafted SiO<sub>2</sub> surface may provide an adsorption reservoir where the  
22  
23 generated formate species on the support surface can spillover on the active PdAg-MnO<sub>x</sub>  
24  
25 domains. Dissociative adsorption of FA and the -NH<sub>2</sub>-facilitated O-H bond scission is followed  
26  
27 by the consecutive C-H bond cleavage from the metal-bound formate intermediate.  
28  
29  
30  
31  
32  
33  
34

35 On the other hand, the lower activity of the catalysts in Figure S11 (see Supporting  
36  
37 Information) with high amine loadings (*i.e.* > 1 mmol NH<sub>2</sub>/g) can be attributed to two main  
38  
39 factors namely, the decreasing particle size of PdAg-MnO<sub>x</sub> NPs on the support surfaces and the  
40  
41 poisoning of the PdAg-MnO<sub>x</sub> NPs by the excessive amount of surface -NH<sub>2</sub> functionalities  
42  
43 covering these NPs. As shown by the TEM images given in Figure S12, PdAg-MnO<sub>x</sub> NP size  
44  
45 distribution can be fine-tuned by changing the coverage of the surface-grafted amine groups.  
46  
47 Figure S12 clearly indicates that the particle size of PdAg-MnO<sub>x</sub> NPs decreases with the increase  
48  
49 in amine concentration. Decreasing particle size may increase the surface concentration of point  
50  
51 defects (*e.g.* corner atoms, kinks etc.) as well as extended defects (*e.g.* steps) on the PdAg-MnO<sub>x</sub>  
52  
53 NPs which may in turn create coordinatively-unsaturated sites with a high affinity towards  
54  
55  
56  
57  
58  
59  
60

1  
2  
3 catalytic poisons such as CO. Similarly, such defect sites may also adsorb other reactants and/or  
4  
5 products in an adversely strong manner disfavoring the Sabatier principle.<sup>46</sup>  
6  
7

8  
9 The influence of the type of the support material was also investigated by synthetically  
10 replacing N-SiO<sub>2</sub> with some of the ubiquitous support materials used in catalysis such as Al<sub>2</sub>O<sub>3</sub>,  
11 TiO<sub>2</sub> and C. The catalytic activities of Pd<sub>0.37</sub>Ag<sub>0.17</sub>-Mn<sub>0.46</sub>/Al<sub>2</sub>O<sub>3</sub>, Pd<sub>0.38</sub>Ag<sub>0.20</sub>-Mn<sub>0.32</sub>/TiO<sub>2</sub>,  
12  
13 Pd<sub>0.40</sub>Ag<sub>0.20</sub>-Mn<sub>0.40</sub>/C and Pd<sub>0.44</sub>Ag<sub>0.19</sub>-Mn<sub>0.37</sub>/N-SiO<sub>2</sub> catalysts prepared by the same method were  
14  
15 investigated in the additive-free FA dehydrogenation under identical conditions (Figure S13).  
16  
17 The activity was observed to decrease in the following order: Pd<sub>0.44</sub>Ag<sub>0.19</sub>-Mn<sub>0.37</sub>/N-SiO<sub>2</sub> (30.8  
18  
19 mL/min) > Pd<sub>0.40</sub>Ag<sub>0.20</sub>-Mn<sub>0.40</sub>/C (10.7 mL/min) > Pd<sub>0.37</sub>Ag<sub>0.17</sub>-Mn<sub>0.46</sub>/Al<sub>2</sub>O<sub>3</sub> (4.32 mL/min) >  
20  
21 Pd<sub>0.38</sub>Ag<sub>0.20</sub>-Mn<sub>0.32</sub>/TiO<sub>2</sub> (2.1 mL/min). The formation of large-sized PdAg-MnO<sub>x</sub> NPs (*i.e.*  
22  
23 sintering) and the lack of -NH<sub>2</sub> functionalities could be responsible for the significantly lower  
24  
25 performances of such catalysts (Figure S14).  
26  
27  
28  
29  
30  
31  
32  
33

#### 34 **Influence of MnO<sub>x</sub> Nanoparticles on Poisoning Resistivity of PdAg Alloy Nanoparticles.**

35  
36 The enhancement of Pd activity in FA dehydrogenation through Ag incorporation has already  
37  
38 been reported for Ag@Pd<sup>18</sup> and PdAg<sup>23</sup> NPs, in which the activity increase has been attributed to  
39  
40 a synergic effect.<sup>47</sup> In order to shed some light on the effect of MnO<sub>x</sub> NPs, we conducted linear  
41  
42 sweep voltammetry (LSV), CO stripping voltammetry and *in-situ* FTIR analyses.  
43  
44  
45

46  
47 (i) *Linear Sweep Voltammetry (LSV) Analyses.* We first performed LSV measurements on  
48  
49 PdAg/N-SiO<sub>2</sub> and PdAg-MnO<sub>x</sub>/N-SiO<sub>2</sub> catalysts to explore their stability in the electro-oxidation  
50  
51 of formic acid. As described in detail in the experimental section, the catalysts were  
52  
53 electrochemically pre-treated before the LSV measurements by using a bias potential of 0.0 V  
54  
55 for 0-180 s, where CO and OH intermediates form and bind to the active surface sites of  
56  
57  
58  
59  
60

1  
2  
3 catalysts.<sup>48- 50</sup> Afterwards, LSV measurements were conducted on the poisoned catalysts  
4  
5 surfaces, in which the maximum current versus potential values was recorded as a function of the  
6  
7 poisoning time (Figure 6 (a) and Figure 6 (b)). It is clearly seen that PdAg-MnO<sub>x</sub>/N-SiO<sub>2</sub> catalyst  
8  
9 has characteristically higher activity than PdAg/N-SiO<sub>2</sub> toward formic acid oxidation in terms of  
10  
11 peak current values. Additionally, investigation of the relative peak current versus poisoning  
12  
13 time (Figure 6 (c)) suggests that although PdAg/N-SiO<sub>2</sub> almost completely loses its initial  
14  
15 activity upon 180 s of poisoning; PdAg-MnO<sub>x</sub>/N-SiO<sub>2</sub> catalyst retains > 85 % of its initial  
16  
17 activity after an identical poisoning treatment.  
18  
19  
20  
21  
22

23 The recent comprehensive <sup>13</sup>C NMR and ATR-IR studies<sup>51</sup> using formate as a surface probe  
24  
25 for metal nanoparticles have shown that (i) adsorption of formic acid on metal nanoparticles  
26  
27 during FA decomposition gives three modes of adsorbed formates; (bridging, linear and  
28  
29 multilinear), and (ii) formate with OCO group, binds to surface metal atoms in a manner very  
30  
31 similar to carbon monoxide. For this reason, as in the case of previously reported works,<sup>52</sup> in  
32  
33 which FA was selectively dehydrogenated to CO<sub>2</sub> + H<sub>2</sub> and no CO was generated, we performed  
34  
35 CO stripping voltammetry and *in-situ* FTIR analyses by using CO as a probe molecule to  
36  
37 understand the influence of MnO<sub>x</sub> on the poisoning resistivity of PdAg alloy nanoparticles.  
38  
39  
40  
41  
42

43 (ii) *CO-Stripping Voltammetry Analyses*. Figure 6 (d) gives CO-stripping voltammograms for  
44  
45 PdAg/N-SiO<sub>2</sub> and PdAg-MnO<sub>x</sub>/N-SiO<sub>2</sub> catalysts (for clarity only 1<sup>st</sup> scans were compared, see  
46  
47 Figure S15 and S16 for complete voltammograms). The onset potentials were found to be 0.30  
48  
49 and 0.23 V for PdAg/N-SiO<sub>2</sub> and PdAg-MnO<sub>x</sub>/N-SiO<sub>2</sub> ( $\Delta V_{\text{COads}} = 70$  mV), respectively. By  
50  
51 considering various previous studies,<sup>52- 57</sup> where even smaller energy differences ( $\Delta V_{\text{COads}} \leq 70$   
52  
53 mV) were reported, this result clearly demonstrates that the CO poisoning resistance of PdAg  
54  
55 alloy NPs can be significantly enhanced by the promotional effect of MnO<sub>x</sub> NPs. Another  
56  
57  
58  
59  
60

significant feature of the CO-stripping voltammograms given in Figure 6(d) is the fact that  $\text{MnO}_x$ -promoted catalyst releases a significantly greater amount of CO during the voltage sweep.

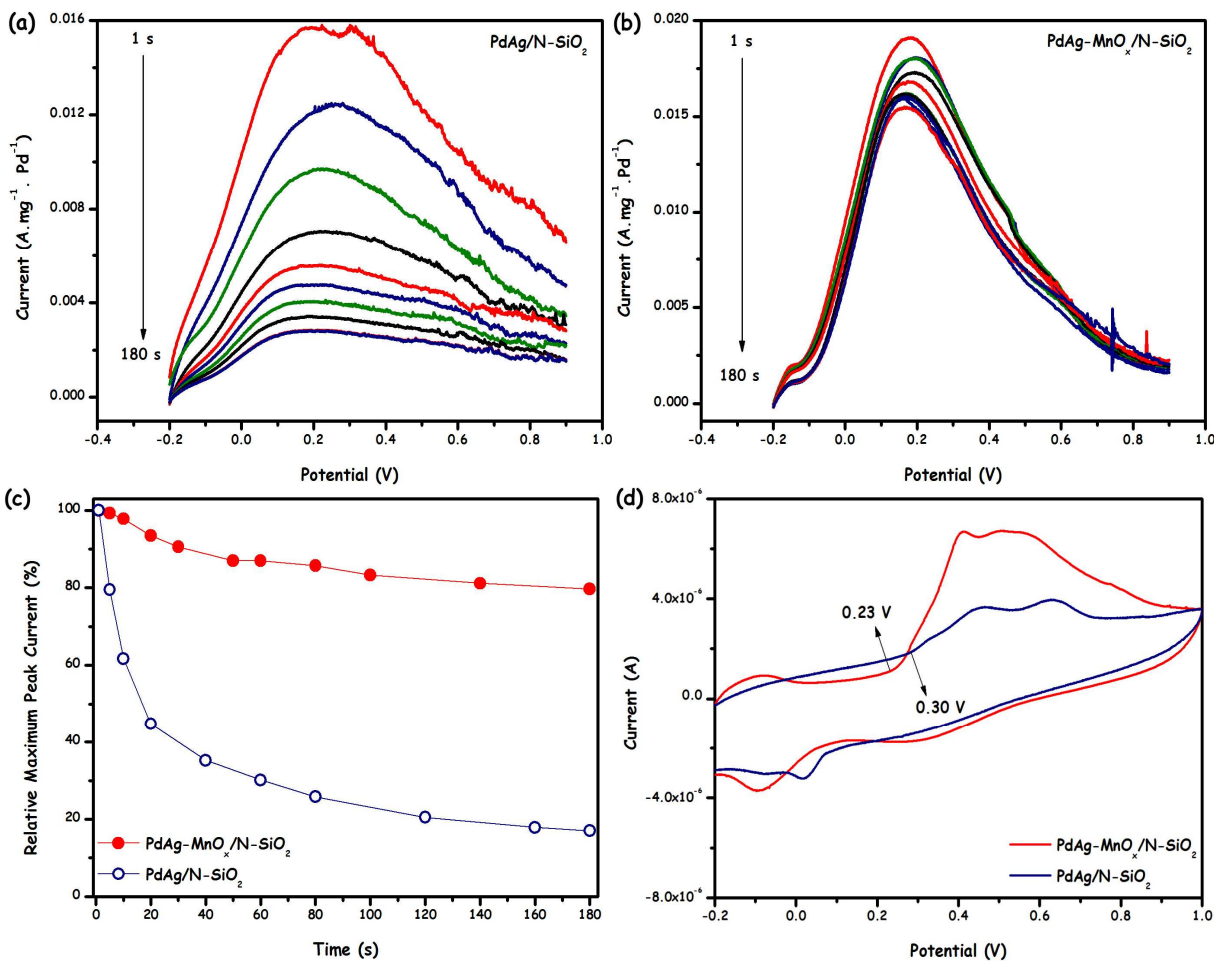


**Figure 6.** LSV measurements on (a) PdAg/N-SiO<sub>2</sub> and (b) PdAg-MnO<sub>x</sub>/N-SiO<sub>2</sub> catalysts in 0.5 M H<sub>2</sub>SO<sub>4</sub> + 1M HCOOH solution with a 10 mV s<sup>-1</sup> scan rate, (c) The relative maximum peak current vs time graph for PdAg/N-SiO<sub>2</sub> and PdAg-MnO<sub>x</sub>/N-SiO<sub>2</sub> catalysts, (d) CO-stripping voltammograms for PdAg/N-SiO<sub>2</sub> and PdAg-MnO<sub>x</sub>/N-SiO<sub>2</sub> catalysts in H<sub>2</sub>SO<sub>4</sub> solution with a 10 mVs<sup>-1</sup> scan rate.

As shown in the Table S1 (see Supporting Information), specific surface area is not the primary factor in CO storage, as MnO<sub>x</sub> incorporation does not significantly alter it. This observation is in perfect agreement with the current *in-situ* FTIR experiments that will be

1  
2  
3 discussed in the forthcoming section suggesting that  $\text{MnO}_x$  domains function as sacrificial sites,  
4 which can efficiently store CO in the form of carbonates, preventing the catalytic poisoning of  
5 the PdAg active sites. It is worth mentioning that in the presence of  $\text{MnO}_x$ , although a  
6 significantly greater quantity of catalytic poisoning species (*i.e.* CO) is captured by the catalyst  
7 surface, these antagonistic species can be very readily and reversibly removed from the catalyst  
8 surface, evident by the lower CO-oxidation onset potential for PdAg- $\text{MnO}_x/\text{N-SiO}_2$  catalysts with  
9 respect to that of PdAg/ $\text{N-SiO}_2$  (Figure 6(d)).  
10  
11  
12  
13  
14  
15  
16  
17  
18  
19

20  
21 (iii) *In-Situ FTIR Spectroscopy.* *In-situ* FTIR experiments were performed (Figure 7) to  
22 investigate the relative CO poisoning characteristics of different adsorption sites on the PdAg-  
23  $\text{MnO}_x/\text{N-SiO}_2$  catalyst at the molecular level. It is well known that Ag and Pd can dissolve in  
24 each other to form bimetallic alloys with a wide range of compositions.<sup>58</sup> Former comprehensive  
25 FTIR spectroscopic studies on supported PdAg bimetallic NPs and PdAg ultrathin films  
26 demonstrated that CO interacts very weakly with the Ag adsorption sites (irrespective of the Ag  
27 content of the bimetallic NP) leading to vibrational features with intensities that are typically  
28 below the experimental detection limit;<sup>59-63</sup> while the interaction of CO with the Pd adsorption  
29 sites is significantly strong. CO vibrational signatures on monometallic Ag NPs deposited on  
30 oxide surfaces typically appear at  $\geq 2169 \text{ cm}^{-1}$ .<sup>64</sup> Before starting to *in-situ* FTIR analyses, the  
31 catalytic reactivity of PdAg- $\text{MnO}_x/\text{N-SiO}_2$  catalyst annealed under vacuum ( $< 1 \times 10^{-3}$  Torr) at  
32 400 K for 2 h was checked in the catalytic dehydrogenation of FA in order to show this  
33 pretreatment does not significantly affect the catalytic nature of PdAg- $\text{MnO}_x/\text{N-SiO}_2$  catalyst.  
34 The result of this control experiment revealed that the catalytic activity of PdAg- $\text{MnO}_x/\text{N-SiO}_2$   
35 catalyst is not affected by this pretreatment as annealed PdAg- $\text{MnO}_x/\text{N-SiO}_2$  catalyst gave almost  
36  
37  
38  
39  
40  
41  
42  
43  
44  
45  
46  
47  
48  
49  
50  
51  
52  
53  
54  
55  
56  
57  
58  
59  
60

1  
2  
3 the same activity and conversion values with that of fresh PdAg-MnO<sub>x</sub>/N-SiO<sub>2</sub> catalyst (Figure  
4 S17).  
5  
6  
7

8  
9 CO adsorption on PdAg reveals unique vibrational features dissimilar to monometallic Pd  
10 surfaces. Pd and PdAg nanoparticles exhibit a truncated-cubo-octahedral geometry (*Wulff*  
11 *Polyhedron*) exposing (111) facets with a minor contribution from (100) facets.<sup>65,66,67</sup>  
12 CO/Pd(111) yields  $\nu_{\text{CO}}$  at *c.a.* 2110, 1960 and 1895-1810 cm<sup>-1</sup> corresponding to atop (linear),  
13 bridging and threefold adsorption geometries, respectively.<sup>66-68</sup> CO/Pd(100) leads to exclusively  
14 bridging adsorption (1997-1807 cm<sup>-1</sup>).<sup>66-67</sup> Figure 7(a) presents *in-situ* FTIR spectra recorded  
15 after the saturation of PdAg/N-SiO<sub>2</sub>, PdAg-MnO<sub>x</sub>/SiO<sub>2</sub> and MnO<sub>x</sub>/SiO<sub>2</sub> surfaces with CO at 323  
16 K. Ag incorporation into the Pd structure strongly alters the CO adsorption on the atop and  
17 bridging Pd sites evident by  $\nu_{\text{CO}}$  at 2045 and 1887 cm<sup>-1</sup> (Figure 7(a)) with a characteristic red  
18 shift ( $\Delta\nu_{\text{CO}} = 65-73$  cm<sup>-1</sup>) compared to that of Pd(111) (*i.e.* 2110 and 1960 and cm<sup>-1</sup>,  
19 respectively<sup>[66]</sup>). This is in perfect agreement with a former study,<sup>69</sup> demonstrating the correlation  
20 between the red-shift in  $\nu_{\text{CO}}$  upon Ag incorporation into the Pd lattice and weakening of the CO  
21 adsorption strength. Similarity in the magnitude of the red shift for atop and bridging Pd  
22 adsorption sites suggests that Ag is rather uniformly distributed in the bimetallic NP, influencing  
23 atop and bridging Pd adsorption sites alike.  
24  
25  
26  
27  
28  
29  
30  
31  
32  
33  
34  
35  
36  
37  
38  
39  
40  
41  
42  
43  
44  
45  
46  
47  
48  
49  
50  
51  
52  
53  
54  
55  
56  
57  
58  
59  
60

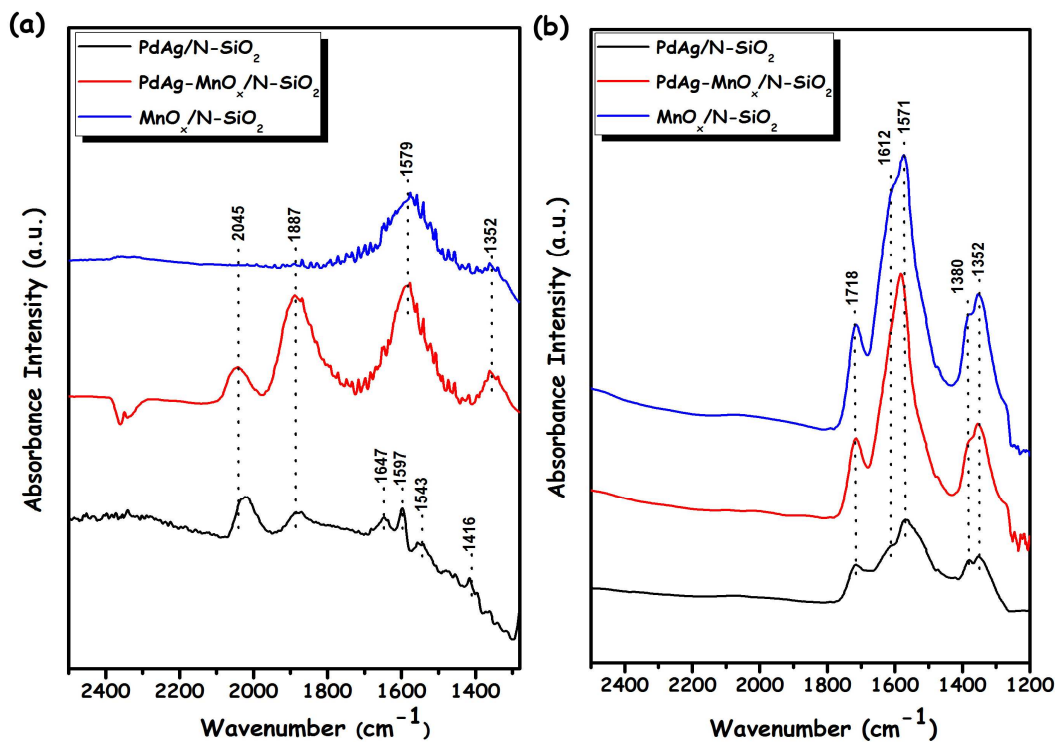


**Figure 7.** (a) *In-situ* FTIR spectra acquired upon CO adsorption (20.0 Torr of CO exposure for 10 min at 323 K) on PdAg/N-SiO<sub>2</sub>, PdAg-MnO<sub>x</sub>/N-SiO<sub>2</sub> and MnO<sub>x</sub>/N-SiO<sub>2</sub>. (b) *In-situ* FTIR spectra acquired upon formic acid adsorption (5.0 Torr of FA exposure for 5 min at 323 K) on CO pre-poisoned PdAg/N-SiO<sub>2</sub>, PdAg-MnO<sub>x</sub>/N-SiO<sub>2</sub> and MnO<sub>x</sub>/N-SiO<sub>2</sub>. All of the spectra were acquired at 323 K in vacuum (10<sup>-3</sup> Torr).

Weakening of the CO adsorption strength is very critical for FA dehydrogenation, as it directly indicates the increased tolerance against CO poisoning. Strongly adsorbed CO on the defective monometallic Pd particles may lead to “*adsorbate-induced surface reconstruction*” resulting in the disintegration (*i.e.* leaching) of the monometallic Pd particles.<sup>59</sup> Decreasing the CO adsorption strength via alloying with Ag increases the stability and catalytic lifetime as demonstrated by the stability and reusability tests (*vide-infra*). Lack of  $\nu_{\text{CO}}$  at  $\geq 2169$  cm<sup>-1</sup> in Figure 7(a) suggests that Ag sites are either not exposed or CO adsorption on Ag is weak. Furthermore, 1887 cm<sup>-1</sup> signal of PdAg-MnO<sub>x</sub>/N-SiO<sub>2</sub> is much stronger than that of the PdAg/N-

1  
2  
3 SiO<sub>2</sub>. In order to explain this observation, one can argue that PdAg NPs located on the MnO<sub>x</sub>  
4 promoted catalyst might have a larger average particle size, thus exposing larger (111) and (100)  
5 facets favoring bridging sites. However, PdAg-MnO<sub>x</sub>/N-SiO<sub>2</sub> does not have a larger average  
6 particle size than PdAg/N-SiO<sub>2</sub> (Supporting Information Figure S5). As an alternative  
7 explanation, variation of the surface composition and surface morphology of the PdAg alloy NPs  
8 upon MnO<sub>x</sub> promotion can be considered. In the presence of MnO<sub>x</sub>, number of exposed Ag sites  
9 on the surface of the bimetallic NPs may decrease, along with the number of coordinatively  
10 unsaturated sites (*i.e.* defects), leading to more ordered (111)/(100) domains and larger (100)  
11 facets on the catalyst surface favoring high-coordination CO adsorption without increasing the  
12 average particle size. It is feasible that CO adsorption on this Ag-doped and ordered (111)/(100)  
13 terraces in proximity of MnO<sub>x</sub> could be energetically less favorable than that of the MnO<sub>x</sub>-free  
14 catalyst. This is in very good agreement with the CO-SV measurements given in Figure 6(d)  
15 suggesting that CO is removed much readily in the presence of MnO<sub>x</sub>. Thus, it is plausible that  
16 MnO<sub>x</sub> domains may modify the surface composition and electronic structure of the PdAg NP  
17 alloy with respect to its MnO<sub>x</sub>-free counterpart.  
18  
19  
20  
21  
22  
23  
24  
25  
26  
27  
28  
29  
30  
31  
32  
33  
34  
35  
36  
37  
38  
39

40 FTIR spectra for CO adsorption on PdAg-MnO<sub>x</sub>/N-SiO<sub>2</sub> and MnO<sub>x</sub>/N-SiO<sub>2</sub> (Figure 7(a))  
41 show two broad and intense features at 1579 and 1352 cm<sup>-1</sup> associated with carbonate species  
42 formed upon adsorption of CO on the Lewis basic sites of MnO<sub>x</sub> and SiO<sub>2</sub>. Weakness of the  
43 carbonate signals in the absence of MnO<sub>x</sub> implies that carbonates are formed almost exclusively  
44 on the MnO<sub>x</sub> domains which act as “*pinning/anchoring sites*” for CO and function as sacrificial  
45 sites against CO poisoning of the precious metal sites. Relatively more intense carbonate features  
46 on PdAg-MnO<sub>x</sub>/N-SiO<sub>2</sub> compared to MnO<sub>x</sub>/N-SiO<sub>2</sub> can be explained by the CO spill-over from  
47 the PdAg NP to the MnO<sub>x</sub> domains. For PdAg/N-SiO<sub>2</sub>, the shoulder at 1850-1700 can be  
48  
49  
50  
51  
52  
53  
54  
55  
56  
57  
58  
59  
60

1  
2  
3 assigned to carbonyls on bridging and threefold sites of PdAg, while features at  $\leq 1650\text{ cm}^{-1}$  can  
4  
5 be attributed to carbonates on N-SiO<sub>2</sub>. Competitive adsorption of FA and CO was also monitored  
6  
7 via *in-situ* FTIR (Figure 7(b)) revealing features at *c.a.* 1718, 1612, 1571, 1380 and 1352  $\text{cm}^{-1}$   
8  
9 assigned to molecular FA<sup>70-72</sup> and bidentate/monodentate formates (HCOO<sup>-</sup>).<sup>70-73</sup> PdAg/N-SiO<sub>2</sub>  
10  
11 shows relatively weak FA/formate features suggesting that strongly-bound CO on PdAg prevents  
12  
13 FA adsorption/formate generation. Carbonates formed on N-SiO<sub>2</sub> also hinder the adsorption of  
14  
15 FA on the support. Thus, in the absence of MnO<sub>x</sub>, CO poisoning severely hinders the FA uptake  
16  
17 capacity. Note that this behavior cannot be explained by differences in surface areas, as the  
18  
19 catalysts in Figure 7 have comparable BET surface area values (Supporting Information Table  
20  
21 S1). PdAg-MnO<sub>x</sub>/N-SiO<sub>2</sub> can absorb a significantly greater quantity of FA/formate even after  
22  
23 extended CO exposure (Figure 7(b)). Incorporation of MnO<sub>x</sub> can provide supplementary  
24  
25 FA/formate adsorption sites, boosting the FA/formate uptake capacity. This is justified by the  
26  
27 control experiments performed on MnO<sub>x</sub>/N-SiO<sub>2</sub> lacking any PdAg (Figure 7(b)). CO capture by  
28  
29 MnO<sub>x</sub> enables the PdAg to remain available for FA adsorption/dissociation where the generated  
30  
31 formates can reversibly spill-over on/from the MnO<sub>x</sub> and N-SiO<sub>2</sub> domains.  
32  
33  
34  
35  
36  
37  
38

## 39 CONCLUSIONS

40  
41  
42  
43 In summary, PdAg-MnO<sub>x</sub>/N-SiO<sub>2</sub> catalyst prepared in this study reveals a remarkable  
44  
45 catalytic performance in terms of activity (330 mol H<sub>2</sub> mol catalyst<sup>-1</sup> h<sup>-1</sup>) and excellent  
46  
47 conversion (> 99 %) in the additive-free dehydrogenation of FA. Moreover, PdAg-MnO<sub>x</sub>/N-SiO<sub>2</sub>  
48  
49 shows excellent stability against agglomeration, leaching and CO poisoning rendering it highly  
50  
51 recyclable and reusable. Incorporation of Ag sites into Pd NPs yields PdAg alloys, decreasing the  
52  
53 CO adsorption strength, increasing CO poisoning tolerance, suppressing the adsorbate (*i.e.* CO)  
54  
55 induced reconstruction and disintegration/leaching of Pd NPs. MnO<sub>x</sub> provides sacrificial CO  
56  
57  
58  
59  
60

1  
2  
3 anchoring sites forming carbonates. As a result, PdAg sites remain available for the  
4  
5 dehydrogenation of FA for an extended duration. This uniquely active, selective and reusable  
6  
7 catalyst has a strong potential to be exploited in practical/technological applications, where FA is  
8  
9 utilized as a viable hydrogen carrier in mobile fuel cell applications.  
10  
11

## 12 13 14 **ASSOCIATED CONTENT**

15  
16  
17 **Supporting Information.** Figures S1-S17 includes information for the catalytic activity tests,  
18  
19 control experiments, CTEM images, CV results and calculation methods. “This material is  
20  
21 available free of charge via the Internet at <http://pubs.acs.org>.”  
22  
23  
24

## 25 26 **AUTHOR INFORMATION**

### 27 28 **Corresponding Author**

29  
30 \* Dr. Mehmet Zahmakiran; E-mail: [zmehmet@yyu.edu.tr](mailto:zmehmet@yyu.edu.tr) ; Fax: 90 432 225 18 06; Website:  
31  
32 [www.nanomatcat.com](http://www.nanomatcat.com)  
33  
34

### 35 36 **Notes**

37  
38 The authors declare no competing financial interest.  
39  
40

## 41 42 **ACKNOWLEDGMENT**

43  
44 MZ thanks to Research Fund of Yüzüncü Yıl University for the financial support to his research  
45  
46 laboratory. Additionally, the partial supports by Fevzi Akkaya Scientific Activities Support Fund  
47  
48 (FABED), Science Academy and Turkish Academy of Sciences (TUBA) are gratefully  
49  
50 acknowledged.  
51  
52  
53

## 54 55 **REFERENCES**

56  
57  
58  
59  
60

- 1  
2  
3  
4  
5 (1) Momirlan, M.; Veziroglu, T. N. *Int. J. Hyd. Energ.* **2005**, *30*, 225-237  
6  
7  
8  
9 (2) Schlapbach, L.; Züttel, A. *Nature* **2001**, *414*, 353-358.  
10  
11  
12 (3) Turner, J. A. *Science* **1999**, *285*, 687-689.  
13  
14  
15 (4) Enthaler, S.; Langermann, J. V.; Schmidt, T. *Energy Environ. Sci.* **2010**, *3*, 1207-1217.  
16  
17  
18  
19 (5) Yadav, M.; Xu, Q. *Energy Environ. Sci.* **2012**, *5*, 9698-9725.  
20  
21  
22 (6) Kordesch, K. V.; Simader, G. R. *Chem. Rev.* **1995**, *95*, 191-207.  
23  
24  
25  
26 (7) Myers, T. W.; Berben, L. A. *Chem. Sci.* **2014**, *5*, 2771-2777.  
27  
28  
29 (8) Zell, T.; Butschke, B.; Ben-David, Y.; Milstein, D. *Chem. A. Eur. J.* **2013**, *19*, 8068-8072.  
30  
31  
32 (9) Wang, W-H.; Xu, S.; Manaka, Y.; Suna, Y.; Kambayashi, H.; Muckerman, J. T.; Fujita, E.;  
33  
34  
35 Himeda, Y. *ChemSusChem* **2014**, *7*, 1976-1983.  
36  
37  
38 (10) Johnson, T. C.; Morris, D. J.; Wills, M. *Chem. Soc. Rev.* **2010**, *39*, 81-88.  
39  
40  
41  
42 (11) Grasemann, M.; Laurenzcy, G. *Energy Environ. Sci.* **2012**, *5*, 8171-8181.  
43  
44  
45 (12) Fukuzimi, S.; Kobayashi, T.; Suenobu, T. *J. Am. Chem. Soc.* **2010**, *132*, 1496-1497.  
46  
47  
48 (13) Boddien, A.; Mellmann, D.; Gaertner, F.; Jackstell, R.; Junge, H.; Dyson, P. J.; Laurenzcy,  
49  
50  
51 G.; Ludwig, R.; Beller, M. *Science* **2011**, *333*, 1733-1736.  
52  
53  
54 (14) Scholten, J. D.; Pechtl, M. H. G.; Dupont, J. *ChemCatChem.* **2010**, *2*, 1265-1270.  
55  
56  
57  
58  
59  
60

1  
2  
3  
4  
5 (15) Zhu, Q. L.; Tsumori, N.; Xu, Q. *Chem. Sci.* **2014**, *5*, 195-199.  
6  
7

8 (16) Zhou, X.; Huang, Y.; Xing, W.; Liu, C.; Liao, J.; Lu, T. *Chem. Commun.* **2008**, 3540-3542.  
9  
10

11 (17) Bi, Q. Y.; Du, X. L.; Liu, Y. M.; Cao, Y.; He, H. Y.; Fan, K. N. *J. Am. Chem. Soc.* **2012**,  
12  
13 *134*, 8926-8933.  
14  
15

16 (18) Tedsree, K.; Li, T.; Jones, S.; Chan, C. W. A.; Yu, K. M. K.; Bagot, P. A. J.; Marquis, E. A.;  
17  
18 Smith, G. D. W.; Tsang, S. C. E. *Nat. Nanotech.* **2011**, *6*, 302-307.  
19  
20

21 (19) Wang, Z. L.; Yan, J. M.; Wang, H. L.; Ping, Y.; Jiang, Q. *J. Mater. Chem. A* **2013**, *1*,  
22  
23 12721-12725.  
24  
25

26 (20) Wang, Z. L.; Yan, J. M.; Ping, Y.; Wang, H. L.; Zheng, W. T.; Jiang, Q. *Angew. Chem. Int.*  
27  
28 *Ed.* **2013**, *52*, 4406-4409.  
29  
30

31 (21) Wang, Z. L.; Yan, J. M.; Ping, Y.; Wang, H. L.; Zheng, W. T.; Jiang, Q. *Chem. Commun.*  
32  
33 **2014**, *50*, 2732-2734.  
34  
35

36 (22) Metin, Ö.; Sun, X.; Sun, S. *Nanoscale* **2013**, *5*, 910-912.  
37  
38

39 (23) Zhang, H.; Metin, Ö.; Su, D.; Sun, S. *Angew. Chem. Int. Ed.* **2013**, *52*, 3681-3684.  
40  
41

42 (24) Bulut, A.; Yurderi, M.; Karatas, Y.; Zahmakiran, M.; Kivrak, H.; Gulcan, M.; Kaya, M.  
43  
44 *App. Cat. B: Env.* **2015**, *164*, 324-333.  
45  
46

47 (25) Yan, J-M.; Wang, Z-L.; Gu, L.; Li, S-J.; Wang, H-L.; Zheng, W-T.; Jiang, Q. *Adv. Energy*  
48  
49 *Mater.* **2015**, *5*, 1500107.  
50  
51  
52  
53  
54  
55  
56  
57  
58  
59  
60

- 1  
2  
3  
4  
5 (26) Yurderi, M.; Bulut, A.; Caner, N.; Celebi, M.; Kaya, M.; Zahmakiran, M. *Chem. Commun.*  
6  
7 **2015**, *51*, 11417-11420.  
8  
9  
10  
11 (27) Gu, X.; Lu, Z-H.; Jiang, H-L.; Akita, T.; Xu, Q. *J. Am. Chem. Soc.* **2011**, *133*, 11822-11825.  
12  
13  
14 (28) Loges, B.; Boddien, A.; Jinge, H.; Beller, M. *Angew. Chem. Int. Ed.* **2008**, *47*, 3962-3965.  
15  
16  
17  
18 (29) Bielinski, E. A.; Lagaditis, P. O.; Zhang, Y.; Mercado, B. Q.; Würtele, C.; Bernskoetter, W.  
19  
20 H.; Hazari, N.; Schneider, S. *J. Am. Chem. Soc.* **2014**, *136*, 10234-10237.  
21  
22  
23 (30) Taylor, I.; Howard, A. G. *Anal. Chim. Acta* **1993**, *271*, 77-84.  
24  
25  
26  
27 (31) White, R. J.; Luque, R.; Budarin, V. L.; Clark, J. H.; Macquarrie, D. J. *Chem. Soc. Rev.*  
28  
29 **2009**, *38*, 481-494.  
30  
31  
32 (32) Chen, W.; Kim, J.; Xu, L-P.; Sun, S.; Chen, S. *J. Phys. Chem. C* **2007**, *111*, 13452-13459.  
33  
34  
35  
36 (33) Jiang, K.; Cai, W. B. *App. Cat. B: Env.* **2014**, *147*, 185-192.  
37  
38  
39  
40 (34) Say, Z.; Vovk, E. I.; Bukhtiyarov, V. I.; Ozensoy, E. *App. Cat. B: Env.* **2013**, *142*, 89-100.  
41  
42  
43 (35) Zhang, Y.; Ouyang, J.; Yang, H. *Sci. Rep.* **2013**, *3*, 1-5.  
44  
45  
46 (36) Prieto, P.; Nistor, V.; Nouneh, K.; Oyama, M.; Lefdil, M. A.; Diaz, R. *App. Surf. Sci.* **2012**  
47  
48 *258*, 8807-8813.  
49  
50  
51 (37) Kang, M.; Park, E. D.; Kim, J. M.; Yie, J. E. *Appl. Catal. A: Gen.* **2007**, *327*, 261-269.  
52  
53  
54  
55 (38) Wang, X.; Kang, Q.; Li, D. *Appl. Catal. B: Env.* **2009**, *86*, 166-175.  
56  
57  
58  
59  
60

- 1  
2  
3  
4  
5 (39) Bondi, J. F.; Oyler, K. D.; Ke, X.; Schiffer, P.; Schaak, R. E. *J. Am. Chem. Soc.* **2009**, *131*,  
6  
7 9144-9145.  
8  
9  
10  
11 (40) Si, P. Z.; Brueck, E.; Zhang, Z. D.; Tegus, O.; Zhang, W. S.; Buschow, K. H. J.; Klaasse, J.  
12  
13 *C. P. Mater. Res. Bull.* **2005**, *40*, 29-36.  
14  
15  
16  
17 (41) Hutchison, J. E.; Woehrie, G. H.; Özkar, S.; Finke, R. G. *Turkish J. Chem.* **2006**, *30*, 1-6.  
18  
19  
20  
21 (42) Li, Y.; Afzaal, M.; O'Brien, P. *J. Mater. Chem.* **2006**, *16*, 2175-2181.  
22  
23  
24 (43) Liu, L.; Liang, H.; Yang, H.; Wei, J.; Yang, Y. *Nanotech.* **2011**, *22*, 015603.  
25  
26  
27 (44) Connors, K. A. *Theory of Chemical Kinetics*; VCH Publishers: New York, **1990**.  
28  
29  
30 (45) Mori, K.; Dojo, M.; Yamashita, H. *ACS Catal.* **2013**, *3*, 1114-1119.  
31  
32  
33 (46) Sabatier, P. *Ber. Dtsch. Chem. Ges.* **1911**, *44*, 1984-1988.  
34  
35  
36  
37 (47) Yoo, J. S.; Pedersen, F. A.; Norskov, J. K.; Studt, F. *ACS Catal.* **2014**, *4*, 1226-1233.  
38  
39  
40 (48) Cai, J.; Huang, H.; Huang, B.; Zheng, S.; Guo, Y. *Int. J. Hyd. Energ.* **2014**, *39*, 798-807.  
41  
42  
43 (49) Zhang, S.; Shao, Y.; Yin, G.; Lin, Y. *Angew. Chem. Int. Ed.* **2010**, *49*, 2211-2213.  
44  
45  
46 (50) Huerta, M. V.; Rodriguez, L.; Tsiouvaras, N.; Pena, M. A.; Fierro, J. L. G.; Pastor, E.  
47  
48 *Chem. Mater.* **2008**, *20*, 4249-4259.  
49  
50  
51 (51) K. Tedsree, A. T. S. Kong, S. C. Tang, *Angew. Chem. Int. Ed.* **2009**, *48*, 1443-1446.  
52  
53  
54  
55  
56  
57  
58  
59  
60

1  
2  
3  
4  
5 (52) Y-L. Qin, J. Wang, F-Z. Meng, L-M. Wang, X-B Zhang, *Chem. Commun.* **2013**, 49, 10028-  
6  
7 10030.  
8

9  
10 Rice, R. I. Masel, A. Wieckowski, *Electrochem. Commun.* **2002**, 4, 599-603.  
11  
12

13  
14 (53) W. Zhou, J. Y. Lee, *Electrochem. Commun.* **2007**, 9, 1725-1729.  
15  
16

17  
18 (54) H. Lee, S. E. Habas, G. A. Somorjai, P. Yang, *J. Am. Chem. Soc.* **2008**, 130, 5406-5407.  
19  
20

21 (55) P. Waszczuk, T. M. Barnard, C. Rice, R. I. Masel, A. Wieckowski, *Electrochem. Commun.*  
22  
23 **2002**, 4, 599-603.  
24  
25

26  
27 (56) C. V. Rao, C. R. Cabrera, Y. Ishikawa, *J. Phys. Chem. C* **2011**, 115, 21963-21970.  
28  
29

30 (57) G. Zhang, Y. Wang, X. Wang, Y. Chen, Y. Zhou, Y. Tang, L. Lu, J. Bao, T. Lu, *App. Catal.*  
31  
32 *B: Env.* **2011**, 102, 614-619.  
33  
34

35  
36 (58) Jingguang, G.C.; Menning, C. A.; Zellner, M. B. *Sur. Sci. Rep.* **2008**, 63, 201-209.  
37  
38

39 (59) Terkhina, O.; Roduner, E. *J. Phys. Chem. C* **2012**, 116, 6973-6979.  
40  
41

42 (60) Heinrichs, B.; Noville, F.; Schoebrechts, J. P.; Pirard, J. P. *J. Catal.* **2000**, 192, 108-118.  
43  
44

45 (61) Soma-Noto, Y.; Sachtler, W. M. H. *J. Catal.* **1974**, 32, 315-320.  
46  
47

48 (62) Huang, W.; Lobo, R. F.; Jingguang, G.C. *J. Mol. Cat. A: Chem.* **2008**, 283, 158-165.  
49  
50

51 (63) Ma, Y.; Diemant, T.; Bansmann, J.; Behm, R. J. *Phys. Chem. Chem. Phys.* **2011**, 13, 10741-  
52  
53 10747.  
54  
55  
56  
57  
58  
59  
60

1  
2  
3  
4  
5 (64) Bechoux, K.; Marie, O.; Daturi, M.; Delahay, G.; Petitto, C.; Rousseau, S.; Blanchard, G.  
6  
7  
8 *Catal. Tod.* **2012**, *197*, 155-160.  
9

10  
11 (54) Henry, C. R. *Sur. Sci. Rep.* **1998**, *31*, 235-240.  
12  
13

14 (66) Ozensoy, E.; Goodman, D. W. *Phys. Chem. Chem. Phys.* **2004**, *6*, 3765-3771.  
15  
16

17  
18 (67) Ozensoy, E.; Min, B. K.; Santra, A. K.; Goodman, D. W. *J. Phys. Chem. B* **2004**, *108*, 4351-  
19  
20 4357.  
21  
22

23 (68) Ozensoy, E.; Vovk, E. I. *Top. Catal.* **2013**, *56*, 1569-1575.  
24  
25

26  
27 (69) Ma, Y.; Diemant, T.; Bansmann, J.; Behm, R. J. *Phys. Chem. Chem. Phys.* **2011**, *13*, 10741-  
28  
29 10746.  
30  
31

32 (70) Millar, G. J.; Rochester, C. H.; Waugh, K.C. *J. Chem. Soc. Far. Trans.* **1991**, *87*, 1491-  
33  
34 1495.  
35  
36

37  
38 (71) Monti, D. M.; Cant, N. W.; Trimm, D. L.; Wainright, M. S. *J. Catal.* **1986**, *100*, 17-24.  
39  
40

41 (72) Burch, R.; Chalker, S.; Pritchard, J. *J. Chem. Soc. Far. Trans.* **1991**, *87*, 193-203.  
42  
43  
44

45 (73) Popova, G. Y.; Chesalov, Y. A.; Sadovskaya, E. M.; Andrushkevich, T. V. *J. Mol. Cat. A:*  
46  
47 *Chem.* **2012**, *357*, 148-159.  
48  
49  
50  
51  
52  
53  
54  
55  
56  
57  
58  
59  
60

